Observed aerosol characteristics to improve forward-modelled attenuated backscatter in urban areas

Observed aerosol characteristics to improve forward-modelled attenuated backscatter in urban areas

Elliott Warren[1*], Cristina Charlton-Perez[2], Simone Kotthaus[1, 3], Franco Marenco[4], Claire Ryder[1], Ben Johnson[4], David Green[5], Humphrey Lean[2], Sue Ballard[2], Sue Grimmond[1*]

[1] Department of Meteorology, University of Reading, UK
[2] Met Office@Reading, UK
[3] Institut Pierre Simon Laplace (IPSL), France
[4] Met Office, Exeter, UK
[5] Environmental Research Group (ERG), King's College London, UK
*Corresponding authors: e.l.warren@pgr.reading.ac.uk, c.s.grimmond@reading.ac.uk

Abstract

Numerical weather prediction (NWP) models often parameterise aerosols to reduce computational needs, while aiming to accurately capture their impact adequately. Increasingly, aerosols are monitored *in-situ* directly and/or indirectly (e.g. by automatic lidars and ceilometers, ALC). ALC measure the aerosol optical characteristic of attenuated backscatter. This can also be estimated using forward models that combine forecast aerosol and relative humidity to parameterise aerosol physical and optical characteristics. The aerFO is one such forward model, designed to use Met Office NWP model output and parameterisations from the MURK visibility scheme. Given the aerFO-MURK scheme link, assessing the aerFO and its output could therefore be used to inform future developments of the MURK scheme. To identify which parameterised physical and optical aerosol characteristics in the scheme are the most critical in urban settings, aerFO is driven with different *in-situ* aerosol observations at a background site in central London. Estimated attenuated backscatter is then assessed against ALC observations. It is shown that the original MURK scheme parameterisation underestimates the variance of both dry mean volume radius and total number concentration. Representing both the accumulation and coarse mode aerosols in the aerFO reduces the median bias error of estimated attenuated backscatter by 69.1 %. Providing more realistic temporal (monthly to hourly) variability of relative mass for different species leads to little improvement, compared to using monthly climatological means. Numerical experiments show that having more realistic estimates of number concentration is more important than providing more accurate values of the dry mean volume radius for the accumulation mode. Hence, improving the parameterisations for number concentration should be a main focus for further development of the MURK scheme. To estimate aerosol attenuated backscatter, the aerFO requires an extinction to backscatter ratio (i.e. the *lidar ratio*). In addition to forward modelling, the lidar ratio can also be used with ALC attenuated backscatter to calculate aerosol properties estimated in aerosol forecasts. Here, a model is developed that estimates the ratio using *in-situ* observations of the number size distribution and speciated aerosol masses. The values of lidar ratio derived at the London background site (14 – 80 sr across selected common lidar wavelengths) compare well to the literature. However, the modelled lidar ratio is unexpectedly correlated to relative humidity. Further, a stronger dependence exists at shorter wavelengths (355 and 532 nm) compared to longer wavelengths (905 and 1064 nm), and is due to the critical relation of lidar wavelength to aerosol size.

Keywords: urban aerosols; lidar forward operator; automatic lidar and ceilometers; urban observation network; lidar ratio

1 Introduction

Forecasting aerosol characteristics accurately is important, due to their impact on radiation budgets and visibility (Roessler and Faxvog, 1981; Seinfeld and Pandis, 2016; Stull, 1988). Understanding the impact of various aerosol characteristics on radiation forecast accuracy would be beneficial for the development of efficient aerosol parameterisations while minimising additional computational resources; as some aerosol species may impact radiation differently.

Currently, it is computationally expensive to use numerical weather prediction (NWP) models with explicit representation of multiple aerosols characteristics, such as mass by species and total number concentration. NWP aims to balance computational cost and forecast accuracy by including aerosol characteristics that are the most critical for the latter. For example, the ECMWF Integrated Forecasting System (IFS) (native resolution up to ~ 9 km) contains mass mixing ratios for sea salt, desert dust, organic matter, elemental carbon and sulphate separately (Benedetti et al., 2009; ECMWF, 2018).

High-resolution Met Office (MO) NWP models, such as the MO UKV (variable resolution 1.5 km inner, 4 km outer domain) (Tang et al., 2013) only explicitly include the total dry mass of bulk aerosol to minimise computational expense (Clark et al., 2008). All other characteristics in the MO UKV, such as number concentration and mass mean radius, are parameterised from the estimated mass through the 'MURK' visibility scheme, which produces a visibility diagnostic from the aerosol characteristics and humidity. Estimating the multiple aerosol characteristics with greater accuracy could help improve MO operational weather forecasts for visibility, and potentially radiation, if aerosol is later coupled to the radiation scheme.

Increasingly, *in-situ* observations in cities include multi-site campaigns to understand spatio-temporal variations in aerosol characteristics, such as particle mass (*PM*, total mass of particulate matter below a given size), size distributions and composition (Crilley et al., 2017; Hama et al., 2017a; Harrison et al., 2012; Klompmaker et al., 2015; Young et al., 2015). Extended routine aerosol monitoring provides further information about inter-annual variability with a wider range of meteorological conditions (Hofman et al., 2016; Ruths et al., 2014); relative importance of aerosol sources in cities that vary both temporarily and spatially with regional background (Abdalmogith and Harrison, 2006); long-range transport (Abdalmogith and Harrison, 2005); and local sources within cities such as transport, construction and fuel burning (Liu et al., 2014; Ye et al., 2013). Interaction between these sources creates a highly diverse aerosol composition with spatial and temporal (hourly to interannual) variations (Stachlewska et al., 2018).

Alongside *in-situ* aerosol observations, automatic lidars and ceilometers (ALC; Wiegner et al., 2014) are being deployed (Flentje et al., 2010; Illingworth et al., 2007; Met Office, 2017; Osborne et al., 2018; Pappalardo et al., 2014). Further, ceilometers are becoming increasingly sensitive with measurements and becoming more comparable to sophisticated lidars, such as Raman (Heese et al., 2010; Madonna et al., 2018, 2014; Song et al., 2017). ALC observations have been used to derive information on aerosol and meteorological conditions, including mixed layer height (Kotthaus and Grimmond, 2018; Wagner and Schäfer, 2015) and in the absence of hydrometeors (cloud, precipitation and fog), relations between attenuated backscatter (β) and *PM* concentrations (Münkel et al., 2004; You et al., 2016). Calibrated and corrected ALC measurements provide the optical property β, rather than a direct measurement of physical aerosol characteristics. Thus, aerosol forward operators (FO) are required to relate aerosol physical properties to β. They allow for attenuated backscatter (β_m) to be estimated from NWP or chemistry transport model output of aerosol parameters for use in model evaluation or in data assimilation (Benedetti and Dabas, 2016; Chan et al., 2018; Charlton-Perez et al., 2016; Geisinger et al., 2017). One such forward operator (hereafter aerFO, Warren et al., 2018), uses a bulk mass of dry aerosol (m) [kg kg^{-1}] and *RH* as inputs, to estimate β_m for clear-sky conditions (i.e. without hydrometeors). aerFO, originally built for the MO MURK visibility scheme (Clark et al., 2008), shares some parameterisations with the MURK scheme to estimate aerosol physical properties but with a revised approach to estimate aerosol optical properties for multiple laser wavelengths.

One important aerosol optical property, the ratio between particle extinction and particle backscatter or lidar ratio (S) (Song et al., 2018), depends on the refractive index and size distribution of the aerosol particles (Müller et al., 2007). S can be used to solve the lidar equation with elastic backscatter lidars, to recover the

particle extinction coefficient (Fernald, 1984; Klett, 1981), or to derive further aerosol properties including aerosol optical depth (AOD) (Seinfeld and Pandis, 2016). *S* has been calculated both directly from Raman lidars (Müller et al., 2007; Papayannis et al., 2005; Wang et al., 2016) or high spectral resolution lidars (Burton et al., 2012; Hair et al., 2008; Reid et al., 2017), and indirectly from sunphotometers (Cattrall et al., 2005). However, all instruments have inherent limitations. Due to the high cost, very few Raman lidars are available and usually they are not operated continuously. Further, they only achieve complete optical overlap several hundred metres above the surface (Li et al., 2016; Wandinger and Ansmann, 2002) so near-surface aerosols are not well observed. Sunphotometers measure AOD, an integrated value for the total atmospheric column, that cannot differentiate near-surface contributions from those aloft. Hence, to derive *S* using a sunphotometer requires additional aerosol modelling (with inherent assumptions) without additional instrumentation (Dubovik and King, 2000). Furthermore, few instruments with the capability to derive *S* are being operated in urban measurement networks because of general constraints such as accessibility, communications and security (Muller et al., 2013). As the lidar ratio in cities is usually lower than for background continental aerosol types (Müller et al., 2007), applying values representative of rural settings may create uncertainty in urban studies of derived aerosol optical properties. Hence, further analysis of urban-based aerosol measurements (i.e. beyond Raman lidars or sunphotometers) could help determine lidar ratio values that are more representative of urban settings. *S* has been derived from aerosol observations using Monte-Carlo analysis with assumed aerosol particle size distributions and refractive indices (Barnaba et al., 2007; Dionisi et al., 2018), though without accounting for aerosol speciation. This may introduce uncertainty as aerosol species have widely varying optical properties (Warren et al., 2018). The Monte-Carlo values are broadly applicable to continental aerosol, but without the temporal variability of aerosol characteristics typical in urban environments (Hama et al., 2017b). A new approach to derive *S* from urban aerosol observations could improve understanding of *S* variability in cities.

This study is structured in two parts. First, a method is presented to estimate *S* at a range of common lidar wavelengths based on in-situ aerosol observations collected at an urban background site. Second, aerFO is used to assess the relative importance of different aerosol properties in the accurate estimation of forward modelled attenuated backscatter (β_m). For this, parameterised aerosol characteristics are successively replaced by more realistic estimates derived from observations. Results can then inform future design of aerosol schemes in MO NWP models with respect to estimating optical properties, by suggesting which aerosol characteristics should be prioritised for inclusion or improvement in the NWP models.

2 Methods

The forward operator, aerFO (Warren et al., 2018), is used to model vertical profiles of attenuated backscatter. Improvements to the aerFO look-up-tables (LUT) (sections 3.1 and Appendix 2) are based on observations taken at North Kensington (NK) (Figure 1, section 2.1).

2.1 Observations

Measurements of attenuated backscatter (β_o), aerosol properties and relative humidity (*RH*) are collected at an urban background site (NK) in the London Air Quality Network (LAQN) (DEFRA, 2018a).

Vertical profiles of β_o are observed with a Vaisala CL31 ALC (*Table 1*), that is part of the London Urban Meteorological Observatory (LUMO; http://micromet.reading.ac.uk/), and has been used in pervious boundary layer studies (Kotthaus et al., 2018, 2016). β_o is corrected for instrument-related background and near-range artefacts (Kotthaus et al., 2016). A centred moving average is applied in time and space, using 25 min windows (101 time steps) and 110 m (11 range gates), to increase the signal to noise ratio (SNR) (section 4.2 in Kotthaus et al., 2016). The CL31 reaches complete overlap at 70 m (Kotthaus et al., 2016). Insufficient optical overlap is corrected for internally by the sensor firmware. β_o from the 2nd range gate is used in this study (20 m above ground level), which is effectively the average of the lowest 7 range gates (70 m). β_o from the 1st range gate is not used given its relatively high noise (Kotthaus et al., 2016).

Calibration coefficients were computed for periods using the 'stratus cloud' method, which has been shown to produce stable estimates (±5 % over 2015) (Hopkin et al., 2019; O'Connor et al., 2004; section 3.1 in Warren et al., 2018). Coefficients produced here are interpolated for days between status conditions with key changes in window transmission, instrument hardware and software changes accounted for. Daily calibration coefficients are applied to the smoothed profiles.

The manufacturer-specified central wavelength of the CL31 is 905 nm. The central wavelength uncertainty is ± 10 nm and full width half maxima (FWHM) is 4 nm (Kotthaus et al., 2016; Wiegner and Gasteiger, 2015). To incorporate this wavelength spectrum into our estimates of aerosol optical properties, we use the FWHM to define a Gaussian weighting function to calculate the dry Mie extinction efficiency ($Q_{ext,dry}$), extinction enhancement factor ($f_{ext,rh}$) with a dependency on *RH*, and the water vapour extinction coefficient ($\sigma_{ext,wv}$) with a dependent on ambient water vapour mass mixing ratio (r_v) (section 2.3 gives an overview of aerFO variables).

Comparison of aerFO-derived β_m and observed β_o is undertaken using seven clear-sky days when all variables (aerosol variables, backscatter and *RH*) are observed, ensuring a fair comparison between all the aerFO experiments.

As no *RH* observations are conducted at the NK site, measurements from a different central London LUMO site (KCL; 6.8 km southeast of NK, Figure 1) are used instead as input to the parameterisation of the swelling and drying of aerosol particles. To assess the representativeness of KCL *RH* measurements at NK, Pearson correlation between two MO UKV NWP model grid boxes containing the respective sites is calculated for hourly *RH* on 30 clear sky days (2014 -2015). *RH* at both locations varied between 40 and 95 % and a good correlation (> 0.99) was found (Table 1).

With measurements of the mass of ammonium sulphate and ammonium nitrate aerosol unavailable, we use the CLASSIC aerosol scheme (Bellouin et al., 2011; Martin et al., 2006) to model this with the observed mass of reactants (Table 2). This assumes the entire ammonium (NH_4) reacts with sulphate (SO_4) preferentially, and only the remaining NH_4 reacts with Nitrate (NO_3). Sea salt mass is calculated from observed Chloride (Cl) mass, assuming all Cl was in sea salt. Ammonium nitrate, ammonium sulphate and sea salt aerosol 15 min mass data are averaged to hourly resolution. To obtain hourly masses of elemental carbon (EC) and organic carbon (OC) the daily masses are linearly interpolated, given the lack of additional information. As EC contains a large fraction of black carbon (strongly absorbing particles, Briggs and Long, 2016), the density and shape factor of black carbon have been used from the literature for EC.

Two aerosol particle diameter size ranges are measured at NK (Table 1):
(i) *Smaller sizes* (0.016 – 0.6 μm): Scanning Mobility Particle Sizer 3081 (SMPS; TSI, 2009) with a Condensation Particle Counter 3775 (CPC; TSI, 2007) operated by King's College London Environmental Research Group (ERG) and National Physics Laboratory (NPL) measures dried particle diameters.
(ii) *Larger sizes* (0.5 – 20 μm): Aerodynamic Particle Sizer 3321 (APS; TSI, 2004) operated by DEFRA. Measurements of ionic components of PM_{10} by an URG-9000B Ambient Ion Monitor (DEFRA, 2018b; URG, 2011) are used to determine ammonium nitrate, ammonium sulphate and sea salt aerosol proportions. PM_{10} is sampled onto filters (Tissuquartz™ 2500 QAT-UP) with a Partisol 2025 sequential air sampler (DEFRA, 2018b; Thermo Fisher Scientific, 2015) and analysed for EC and OC using a Sunset Laboratory thermal–optical analyser according to the QUARTZ protocol (with very similar results to EUSAAR 2: Cavalli et al., 2010) (Beccaceci et al., 2013). Particles measured at ambient *RH*.

Table 1: Observations from North Kensington (NK) (Figure 1) operated by LUMO (Kotthaus and Grimmond, 2018, 2014) *and Environmental Research Group (ERG) LAQN (Mittal et al., 2016). † Particle number distribution data from two instruments (by diameter size) are combined to extend the range of particle sizes used to estimate aerosol optical properties (section 2.3). * RH from King's College London (KCL) is used.*

Variables		Instrument	Sampling	Period	Source
Attenuated backscatter β_o		Vaisala CL31	15 s, 10 m	01/01/2014 – 31/12/2015	LUMO NK
PM_{10} by species	Ammonium sulphate [$(NH_4)_2SO_4$]	URG-9000B AIM	15 min	02/02/2011 – 07/02/2018	ERG/ NPL NK
	Ammonium nitrate [NH_4NO_3]		15 min		
	Sea salt [NaCl]		15 min		
	Elemental carbon (EC)	Partisol 2025/Sunset	Daily		
	Organic carbon (OC)		Daily		
Particle number distribution †		SMPS 3081 (with CPC 3775)	~0.016 – 0.6 µm, 51 size bins (small)	01/01/2014 - 31/12/2015	ERG/ NPL NK
		APS	~0.5 – 20.0 µm, 52 size bins (large)	01/01/2014 – 31/12/2015	ERG UK
Relative Humidity *RH* *		Vaisala WXT520	5 s	01/01/2014 – 31/12/2015	LUMO KCL

*Table 2: Aerosol species modelled: ammonium sulphate, ammonium nitrate and sea salt. Mass calculated from respective reactants observed. † Elemental carbon assumed to be completely hygrophobic. * Efflorescence and deliquescence limits taken from swelling method source. Varutbangkul et al. (2006) found no efflorescence or deliquescence limits for organic carbon. ^ shape factor (χ) used if particles are on the 'dry' branch of the hysteresis curve. See Table 1 for aerosols species. Sources: Fi75 Fitzgerald (1975) Sc07 Schkolnik et al. (2007), SP16 Seinfeld and Pandis (2016), Va06 Varutbangkul et al. (2006), Ze06 Zelenyuk et al. (2006), Zh16 Zhang et al. (2016),*

Aerosol species	Estimated from observed reactants	Swelling method applied	Efflorescence * relative humidity [%]	Deliquescence * relative humidity [%]	Dynamic shape factor		Density	
					χ ^	Source	ρ_p [kg m^{-3}]	Source
$(NH_4)_2SO_4$	NH_4, SO_4	Fi75	30	81	1.0	SP16	1770	n/a
NH_4NO_3	NH_4, NO_3	Fi75	30	61	1.0	n/a	1720	n/a
OC	n/a	Va06	n/a	n/a	1.0	Ze06	1100	Sc07
EC	n/a	n/a †	n/a	n/a	1.2	Zh16	1200	Zh16
NaCl	Cl	Fi75	42	75	1.08	SP16	2160	n/a

The SMPS and APS datasets together cover a large range of particle sizes, enabling a more representative estimate of aerosol physical and optical properties to be derived. Unfortunately, the SMPS and APS observe aerosol particle diameters in slightly different ways. The SMPS provides the mobility diameter (D_m) or particle diameter relative to a perfect sphere with the same electrical mobility in a constant electrical field (DeCarlo et al., 2004). The APS provides aerodynamic diameter (D_a) or diameter relative to an aerodynamic property measured (DeCarlo et al., 2004). Therefore, to merge these datasets together, both are first converted to a common particle size, i.e. the volume equivalent diameter (D_v). D_v is based on particle surface area, and chosen as it is more closely related to aerosol optical properties (e.g. extinction coefficient) than D_m or D_a (Seinfeld and Pandis, 2016). The diameter conversions to D_v are done prior to computing particle optical properties based on Mie theory.

The diameter conversion equations require additional aerosol parameters that can vary slightly by species (*Table 2*). For instance, the dynamic shape factor (χ) is used to convert D_m or D_a and the particle density (ρ_p) is required to convert D_a to D_v. χ describes the sphericity of a particle: $\chi = 1$ for a perfect sphere and $\chi > 1$ for non-spherical particles (Hinds, 1999). Often the Cunningham slip correction factor (C_c) is used when converting between equivalent diameters to account for the no-slip condition for small particles (Seinfeld and Pandis, 2016). However, we assume C_c can be ignored given the contribution by small particles (< ~ 0.07 µm) to the optical properties of total aerosol is negligible (section 3.2).

From the merged number distribution, three aerosol mode ranges are defined (D_v: fine < 0.08 µm; accumulation 0.08 – 0.8 µm; coarse > 0.8 µm). These are interpreted based on the mean dV/dlogD of the dry particle number distribution (where V is the volume) between 01/01/2014 – 31/12/2015 at NK.

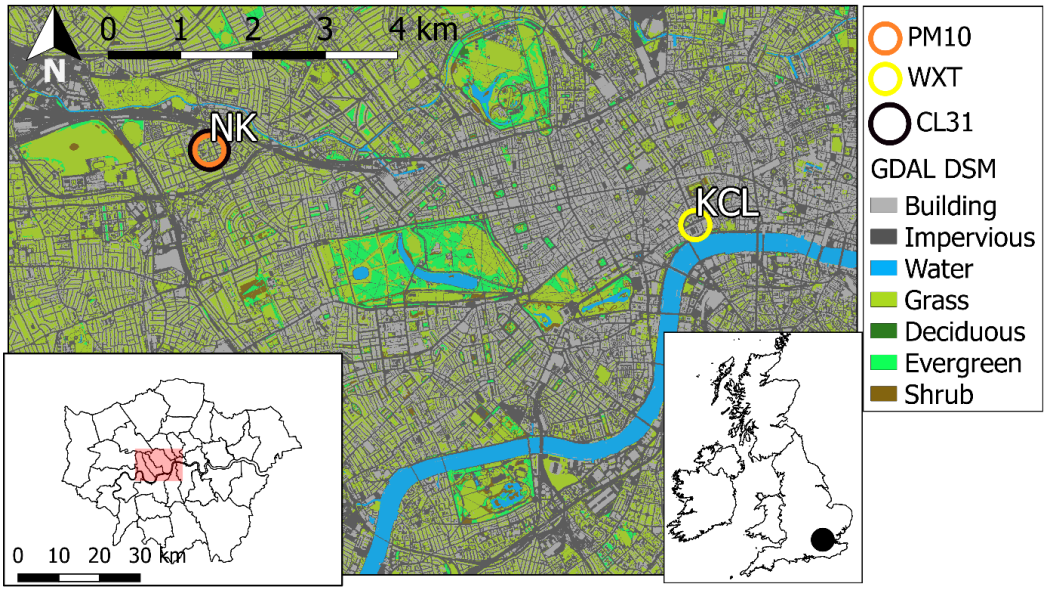

Figure 1: LUMO (CL31, WXT) and LAQN measurement sites in central London and surface cover type (data source described in Lindberg and Grimmond, 2011); within Greater London and the British Isles (insets).

2.2 Using observations to model the lidar ratio (S)

The extinction-to-backscatter ratio, or lidar ratio *S*, is a key component of aerFO as it links the modelled extinction to the modelled backscatter. As is common (Doherty et al., 1999; Müller et al., 2007), Warren et al. (2018) assumed a constant value (S = 60 sr^{-1} typical of continental aerosol) to estimate β_m from σ_{ext} in aerFO. Here, a more detailed parameterisation is developed to model *S* (e.g. for use in aerFO) using aerosol observations of particle size distribution, speciated aerosol mass and *RH*.

To estimate *S* (Figure 2), the overall approach is to model the aerosol optical properties based on the aerosol physical properties, including the observed dry number distribution by aerosol species ($N_{aer}(D)$) binned by diameter (D). The extinction and backscatter properties for each aerosol species (Table 2) are modelled separately, assuming an external aerosol mixture. Hygroscopic growth and consequential changes in the complex index of refraction of each aerosol species, from additional water, are also parameterised.

Initially, with only non-speciated observations of dry number distribution by diameter ($N_{obs}(D)$) available, $N_{aer}(D)$ are estimated by speciating $N_{obs}(D)$ using observed hourly PM_{10} mass of different aerosol types (m_{aer}, Figure 2, part 1). m_{aer} is used with observed aerosol density of each species from the literature (ρ_{aer}, Table 2) to create volumetric weights ($V_{weight,aer}$; ratio of each species (V_{aer}) to total aerosol (V_{tot}) volume). The $V_{weight,aer}$ provide *a priori* weights for each bin of $N_{obs}(D)$ to obtain $N_{aer}(D)$ *by* species:

$$N_{aer} = N_{obs}(V_{aer}/V_{tot}) \quad (1)$$

After estimating $N_{aer}(D)$ for each species, the hygroscopic effects on aerosol particles are parameterised. As *RH* increases, hydrophilic aerosol particles swell (i.e. increase in size) with water, and the complex index of refraction changes, reaching some state between that of a dry particle and a water droplet (Haeffelin et al., 2016). For hydrophilic species, the parameterised physical growth of each binned diameter follows the CLASSIC aerosol scheme (Bellouin et al., 2011) such that the swollen diameters $D_{wet,aer}$ and dry diameters $D_{dry,aer}$ are calculated using ambient *RH*. In this study, the hygroscopic parameterisations require the observed dry SMPS particle sizes to be swollen to find $D_{wet,aer}$, and the observed humidified APS particle sizes to be dried to find $D_{dry,aer}$. Once $D_{dry,aer}$ and $D_{wet,aer}$ for the merged number distribution are calculated, the physical growth factor g_{aer} is estimated (Figure 2 part 2). g_{aer} is used with the size parameter X_{aer} (eqn. 15.6 in Seinfeld and Pandis, 2016) for each size bin and each species, to estimate the mixed complex index of refraction between that of dry aerosol and of pure water ($n_{wet,aer}$) using the volume mixing method (Liu and Daum, 2008). Once $D_{wet,aer}$ and the mixed complex index of refraction are calculated, Mie scattering code is used with the swollen particles to calculate the optical properties: extinction and backscatter efficiencies ($Q_{ext,aer}$, $Q_{back,aer}$), and extinction and backscatter cross-sections ($C_{ext,aer}$, $C_{back,aer}$). The Mie scattering code used was written with the pymiecoated module for Python 2.7 (version 0.1.1: https://code.google.com/archive/p/pymiecoated/). Following this, the total extinction and backscatter for each aerosol species ($\sigma_{ext,aer}$, $\sigma_{back,aer}$) is calculated using $N_{aer}(D)$ with $C_{ext,aer}$ and $C_{back,aer}$, respectively. The sum of $\sigma_{ext,aer}$, and $\sigma_{back,aer}$ is used to compute the overall σ_{ext} and β. Finally, *S* is computed as the ratio of σ_{ext} to β (Figure 2, part 3).

As optical properties of aerosol particles are highly sensitive to particle size (Jacobson, 2005), the number and arbitrary position of diameter bins in the observed number distribution can affect the final modelled $\sigma_{ext,aer}$, $\sigma_{back,aer}$ and *S* results. To minimise the impact of number and arbitrary bin diameter sizes on optical property results, we follow Geisinger et al. (2017 section 2.2.4) in part 2 (Figure 2). This increases the total number of diameter bins by a factor of 4, by interpolating between the adjacent diameter bins. X_{aer} and $n_{wet,aer}$ are calculated for each interpolated bin, and the optical properties for each original bin (D_i) are derived as the average of the interpolated bins for that size interval.

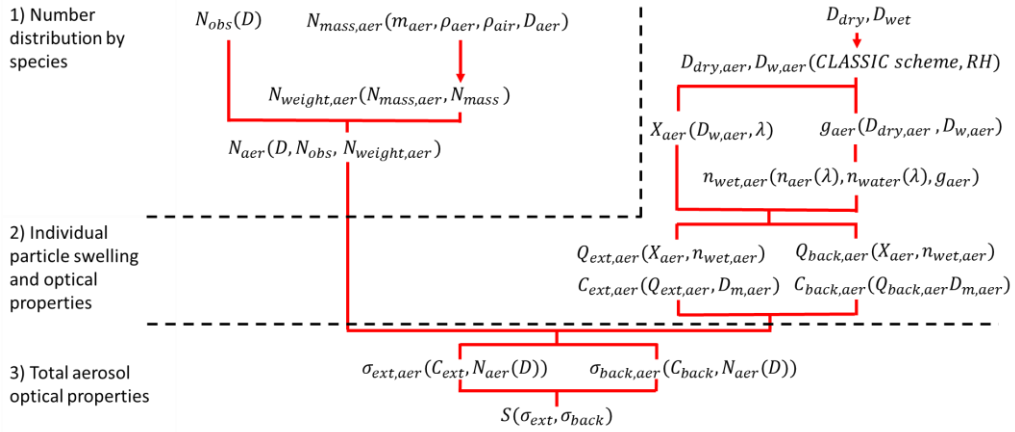

Figure 2: Lidar ratio (S) calculation flow chart. The main inputs are diameter bins (D), number distribution by diameter ($N_{obs}(D)$), and aerosol species mass at a given size range (m_{aer}), e.g. PM_{10}, and relative humidity (RH). See section 7 for notation.

For some particles (both pure and mixed species aerosol), particle hygroscopic growth has been observed to exhibit hysteresis (Figure 3) with a differing shrinking and growing relation with changes in *RH* (Fierz-Schmidhauser et al., 2010; Tang and Munkelwitz, 1994). Thus, these particles have no simple relation between *RH* and their extinction coefficient). For example, many particles that are originally dry, solid and without any water condensation on them, can be defined as being below their efflorescence *RH* limit and on the lower branch (Figure 3, red). Particles already swollen through hygroscopic growth that are liquid solutions containing aerosol, can be defined as being above their deliquescent *RH* limit and on the upper branch (Figure 3, blue). When ambient conditions change so that *RH* is between these limits, the particles may not shrink or swell until they reach the other *RH* limit (Figure 3, grey). Particles originally above the deliquescence *RH* limit, may remain relatively large, despite a decrease in *RH* until the critical efflorescence limit is reached at which point the particle suddenly crystallises and loses all remaining condensed water (Tang and Munkelwitz, 1994). Conversely, dry particles below the efflorescence *RH* limit may stay dry and solid as ambient *RH* increases until reaching the deliquescent *RH* limit, then suddenly swell with water.

Given the importance of particle size on aerosol optical properties, the hysteresis effect was incorporated into the model to estimate *S*. The magnitude of the hysteresis effect for ambient aerosol varies (Figure 5 in Fierz-Schmidhauser et al., 2010). Therefore, we parameterise the hysteresis effect for ammonium sulphate, ammonium nitrate and sea salt separately (Figure 3). Originally dry particles (begin below efflorescence limit: Table 2) did not swell and were treated as being in a 'dry' crystalline state (s_1, s_2). Once *RH* exceeds the deliquescence limit (per aerosol type) the parameterised particles are considered to be in a 'wet' liquid state (s_3, s_4) and their growth follows the aerosol type swelling method (Table 2). While in the 'wet' state, growth of particles continues due to swelling until *RH* falls below the efflorescence limit. Particles then return to a 'dry' state and no swelling method is applied. Hysteresis is not assumed for OC as its efflorescence and deliquescence limits are unclear and the hygroscopic growth has been observed to be smooth without an apparent hysteresis (Varutbangkul et al., 2006).

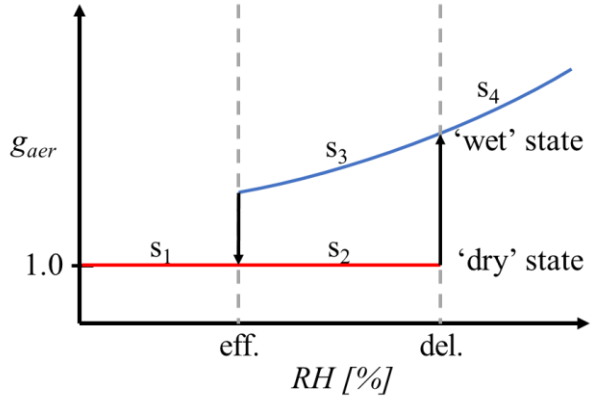

Figure 3: Schematic of the particle physical growth factor (g_{aer}) hysteresis with RH. A particle is assumed to be in either a dry (s_2) or wet (s_3) state when between the efflorescence (eff) and deliquescence (del) RH limits. 'Dry' particles at s_1 move to s_2. Once the ambient RH reaches the deliquescence RH limit particles move from s_2 to the s_4 branch. 'Wet' particles at s_4 move to s_3 and once the ambient RH reaches the efflorescence RH limit the particles have a dry branch response (s_1). This is based on observations presented in Table 2.

2.3 Overview of aerFO

For a complete description of aerFO see Section 2 of Warren et al. (2018). aerFO is designed to estimate clear-sky β_m, using bulk mass of dry aerosol (m) [kg kg^{-1}] and *RH* from NWP as inputs. However, observations can also be used. Clear-sky conditions are defined as sub-saturated conditions based on the input *RH*, where no hydrometeors, such as cloud, fog or rain impact β_m, and where β_m is dominated by aerosol backscatter.

Initially, aerFO estimates the bulk aerosol physical properties of the aerosol accumulation mode, including dry mean radius (r_{md}) and total number concentration (N) using observed and empirically derived constants (Figure 4, part 1). These include the climatological mean dry mass of aerosol (m_0), climatological mean volume mean radius for the aerosol mode (r_0), climatological mean total number concentration for the aerosol mode (N_0) and a scaling factor (p). Following the MO visibility scheme (Clark et al., 2008) for the parameterisations of N and r_{md} a fixed geometric standard deviation (d_g) of 1.7 is used for the accumulation mode as calculated from observations. Properties calculated include: aerosol optical (e.g. $Q_{ext,dry}$ and σ_{ext}; Figure 4, parts 2 – 3), backscatter and transmission (Figure 4, part 4). aerFO can represent multiple aerosol modes (e.g. fine, accumulation and coarse) by calculating $\sigma_{ext,aer}$ (Figure 4, parts 1 – 2) for each mode and adding them to obtain the overall $\sigma_{ext,aer}$. The effect of water vapour absorption ($\sigma_{ext,wv}$) is also included in the total extinction coefficient (σ_{ext}).

For computational efficiency, $Q_{ext,dry}$ and $f_{ext,rh}$ (Figure 4, part 2) are pre-calculated for aerFO. As the relative composition of aerosols may vary (e.g. by month Young et al., 2015), a monthly climatology of urban aerosol composition is derived from NK aerosol observations (Table 2, section 2.1).

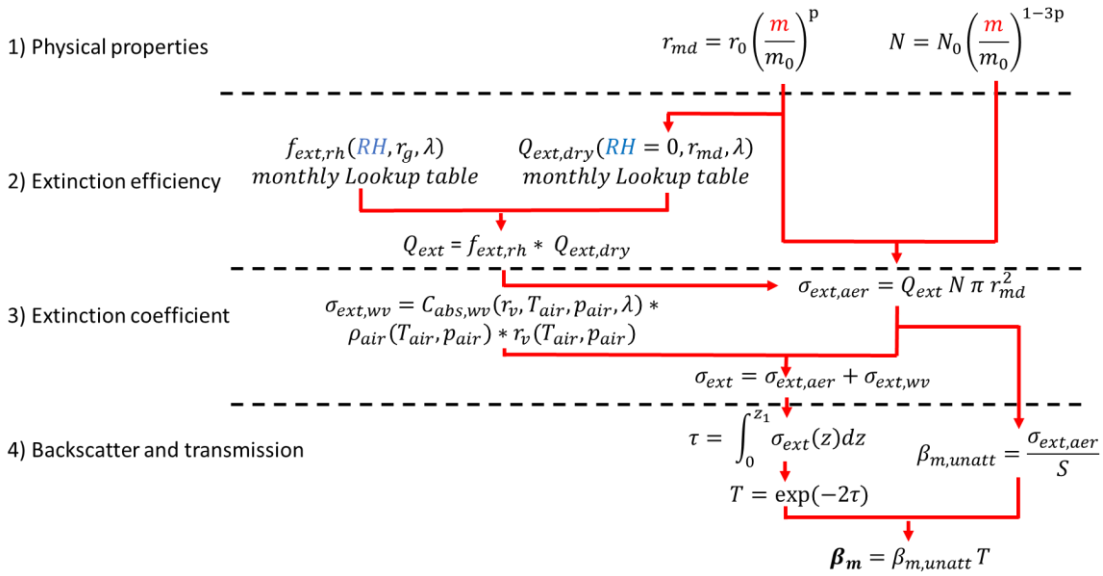

Figure 4: The aerosol forward operator (aerFO) to estimate attenuated backscatter from the NWP inputs of aerosol mass mixing ratio (m) and relative humidity (RH). See section 7 for notation. Modified from: Warren et al. (2018)

Look up tables (LUT) are derived for $f_{ext,rh}$ based on the geometric mean radius (r_g), using SOCRATES (Manners et al., 2015) Mie scattering code within the radiation suite. r_g is estimated from r_{md} using linear regression based on observations for the aerosol accumulation mode. Relations between r_{md} and r_g are derived for each aerosol mode separately (e.g. fine, accumulation and coarse mode in experiment 5; section 3.2).

N_0 is highly sensitive to the defined size range of the accumulation mode (Warren et al., 2018). Therefore, the default aerFO N_0 and the mean dry volume radius (r_0) are re-calculated for NK, from the mean observed particle number distribution for the accumulation mode (Table 3) from the SMPS and APS measurements (*Table 1*).

Table 3: Default input parameters for aerFO at NK (Figure 1) using all available data.

Site (type)	Accumulation radius size range [μm]	N_0 [cm^{-3}]	r_0 [μm]
NK (urban background)	0.04 – 0.4	1311	0.159

2.4 Aerosol forward operator experiments

The improvement in β_m estimates when using observed aerosol characteristics (e.g. size, total number) is evaluated using a set of aerFO experiments (Table 4). For these we use observations (rather than NWP model forecasts) as inputs to aerFO. As observations replace parameterised variables, β_m is changed (Figure 4, part 1). For comparison, we define a control run (ID = 0, Table 4), with physical properties N and r_{md} (Figure 4, part 1) estimated based on aerFO parameterisations, with measured PM_{10} mass and RH (Table 1). In experiments 1 – 7 parameterised variables (e.g. N and r_{md}) are replaced by estimates from aerosol observations (Table 4). Experiments 1 – 3 consider the accumulation mode whereas experiments 4 – 7 address multiple aerosol modes (e.g. fine, accumulation and coarse).

Parameterised N is replaced by observed N for the accumulation mode (ID = 1); observed r_{md} for the accumulation mode is used (ID = 2); both observed N and r_{md} are provided (ID = 3) to eliminate the need for a mass estimate as input to aerFO. Each subsequent experiment (ID > 3) uses more observations and accounts for more aerosol modes. Using observed N and r_{md} for two (accumulation and fine) aerosol modes (ID = 4) allows assessment of the importance of the fine mode to accurately calculate the aerosol optical properties. To represent multiple modes in aerFO (Figure 4, parts 1 -3) each mode is treated separately when obtaining the extinction coefficient. Experiment 5 uses observed N and r_{md} for the fine, accumulation and coarse aerosol modes. Experiment 6 is as 5, but with hourly aerosol composition used to calculate hourly varying $Q_{ext,dry}$ and $f_{ext,rh}$ LUT. Experiments 0 – 6 use a mean S (section 2.2), whereas 7 is as 6, but with hourly estimates of S.

The experiments are limited to seven clear-sky days (in 2014: 06/06; 03/07; and 2015: 07/03; 20/04; 21/04; 04/06; 02/08) by the limited simultaneous data availability of all measurements Although the evaluation of β_m is done at 905 nm, β_m can be computed for other ALC wavelengths (e.g. 355, 532, 1064 nm) but is not assessed as observations at other wavelength are unavailable.

*Table 4: Experiments (ID) assumptions for number concentration (N) and optical properties as input to aerFO with which aerosol characteristics are replaced with observations measured at NK (Figure 1). All aerFO experiments use observed RH from KCL. Mode diameter ranges: < 0.08 μm (fine), 0.08 – 0.8 μm (accumulation) and > 0.8 μm (coarse). * control run. See section 7 for notation.*

ID	Aerosol variables estimated based on observations	Aerosol observations used
*0**	$m = PM_{10}$	Particle mass
1	N (accumulation mode)	Particle number distribution (fine and coarse)
2	r_{md} (accumulation mode)	
3	N, r_{md} (accumulation mode)	
4	N, r_{md} (fine and accumulation mode)	
5	N, r_{md} (fine, accumulation and coarse mode)	
6	N, r_{md} (fine, accumulation and coarse mode), $Q_{ext,dry}$, $f_{ext,RH}$	Particle number distribution (fine and coarse) and mass by species
7	N, r_{md} (fine, accumulation and coarse mode), $Q_{ext,dry}$, $f_{ext,RH}$, S	

3 Results

3.1 Lidar ratio (S) sensitivity to aerosol type and size

Aerosol lidar observations are commonly conducted at typical Raman lidar channels (e.g. 355, 532 nm) or at the wavelengths used by ALC (e.g. 905, 1064 nm). To account for differences in lidar wavelengths, the lidar ratio S is estimated from aerosol observations at NK at these four wavelengths (Figure 5). Across all wavelengths S varies between ~14 – 80 sr. This wide range of S and corresponding β (not shown) are similar to those obtained using aerosol characteristics with Monte-Carlo methods (Barnaba et al., 2007; Dionisi et al., 2018). The 905 nm S average of 43.1 sr is similar to that measured in urban areas by Raman lidars (Müller et al., 2007; Stachlewska et al., 2018; Wang et al., 2016), but is low compared to that derived using sunphotometer observations (Cattrall et al., 2005).

To date, there is little published research on the relation between S and RH. S generally has a positive linear relation to RH. This is strongest at ALC wavelengths 905 and 1064 nm (Pearson correlation of 0.83 and 0.78, respectively). The dependence of S on RH (Figure 5) is linked to the relation between the aerosol size distribution and S, and likely to the relative position of the accumulation mode size range (Figure 6). For OC and any particles in the 'wet' deliquescent state (section 2.2), particles swell or shrink in response to changing RH, as water vapour condenses onto or evaporates from them. Consequently, particles move up or down the curve (Figure 3). Many particles in the particle size distribution lie within the accumulation mode, and the smaller half of the accumulation mode, are on a monotonic part of the curve, before the first inflection point (e.g. ~ 0.2 μm at 355 nm for most aerosol types). For these particles, changes in RH, and subsequent changes in particle size, lead to monotonic changes in S.

In the accumulation mode size range (diameter: 0.08 – 0.8 μm), the number of inflection points varies with wavelength for all aerosol species considered (Figure 6). At the longer 905 and 1064 nm wavelengths (Figure 6c, d), the first local maximum of S is associated with larger particles compared to the Raman channels (Figure 6a, b) so there are fewer inflection points across the accumulation size range (Figure 6, dashed lines). At shorter wavelengths (355, 532 nm) there are more inflection points within the accumulation range causing a more variable response (greater scatter) of S to changes in RH (Figure 5a, b).

Additionally, S is influenced by the proportions of aerosol species at some wavelengths and humidities. At 355 (Figure 7) and 532 nm (not shown) and at low RH, S increases with greater relative EC abundance as EC absorbs radiation more efficiently than other aerosol types. However, when RH increases, the relation between EC and S is less clear which could be because the other hygroscopic aerosol types may be in the 'wet' deliquescent state, have swollen and increased their size. Consequently, the swollen hygroscopic aerosol S values increase to a magnitude like or above those of dry (un-swollen) EC. Though the relation between EC and S is most pronounced at shorter wavelengths, it is unclear at longer wavelengths including at low RH (905, 1064 nm; not shown). In addition to the impact of aerosol proportion on S, a clear impact is found for $f_{ext,rh}$ at 355, 532, 905 and 1064 nm (905 nm shown in Appendix 2).

Some assumptions made in calculating S may reduce S variability with changing RH (Figure 5). Applying Mie theory based on spherical particles might limit variability in S of both EC and hygroscopic particles at low RH before the hygroscopic particles become swollen (i.e. pre-spherical). Speciating $N(D)$ evenly across all bins based on the total mass of each species available (section 2.2) likely does not portray the actual diversity in size distributions. This simplification does not allow individual species to contribute more to one specific mode; for example, sea salt could contribute more to the coarse mode.

In the parameterisation of S (Figure 2) internal aerosol mixing is not considered. This would lead to a wide range of efflorescence and deliquescence RH limits for different particles and hence change the particle physical growth factor with respect to water (g_{aer}). Omitting internal mixing likely means hysteresis-related variability is not fully represented. In laboratory conditions Fierz-Schmidhauser et al. (2010) found a clear hysteresis effect on enhanced scattering from several pure aerosol species, but in field conditions with ambient aerosol hysteresis it was not always detected. Similarly, Smith et al. (2012) found that varying the fractions of organic material to ammonium sulphate changed the efflorescence and deliquescence RH limits of ammonium sulphate greatly, with any apparent RH limits eliminated once organic material volume fractions exceeded 0.6.

Evaluation of β_m (section 3.2) uses several different parameterisations of S (e.g. linear regression with RH) to help identify which should be the default in aerFO. Given this evaluation (not shown), as well as the remaining uncertainty and various causes for variability in estimating S, the mean S for each wavelength is used as the default value in aerFO. The mean S for 905 nm is 43.1 sr (median 44.1 sr), calculated from a sample size of 4699 hours (across 17 months in 2014 – 2015).

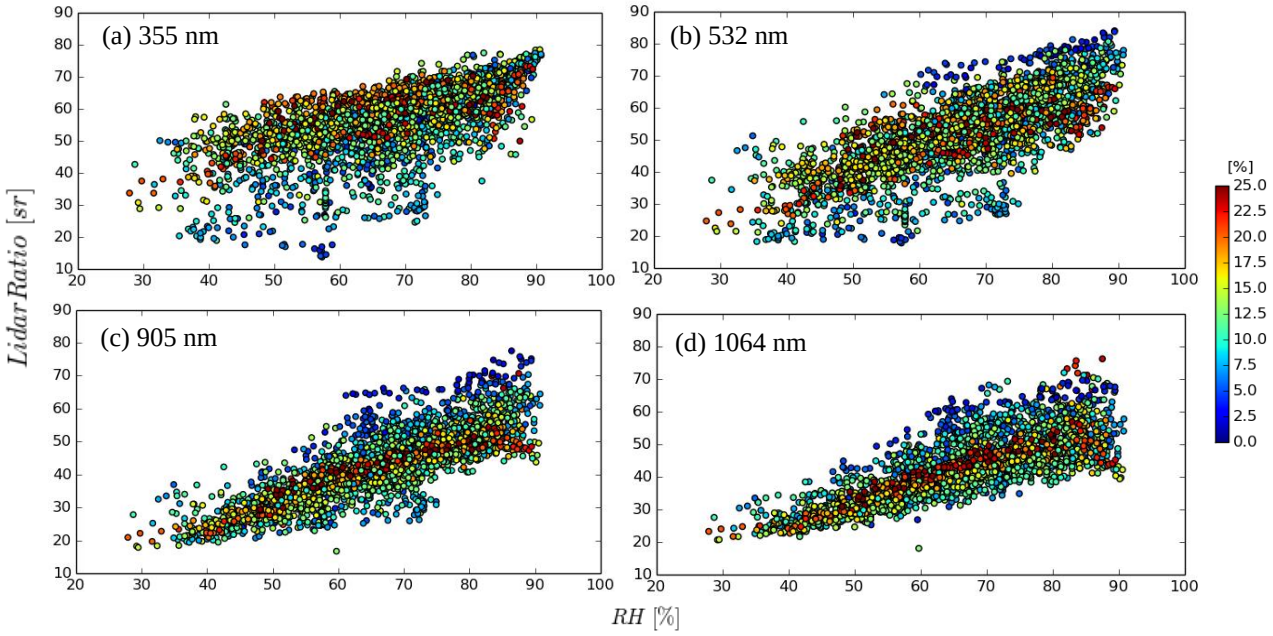

Figure 5: Calculated lidar ratio (S, sr, Figure 2) as a function of relative humidity (RH) [%] and elemental carbon proportion of total aerosol (%, colour) at four wavelengths that are typical of: Raman lidar (a) 355, (b) 532 nm; and ALC (c) 905 (Vaisala CL31) and (d) 1064 nm (Lufft CH15MK). Calculated hourly using NK (Figure 1) data for the period 01/01/2014 – 31/12/2015.

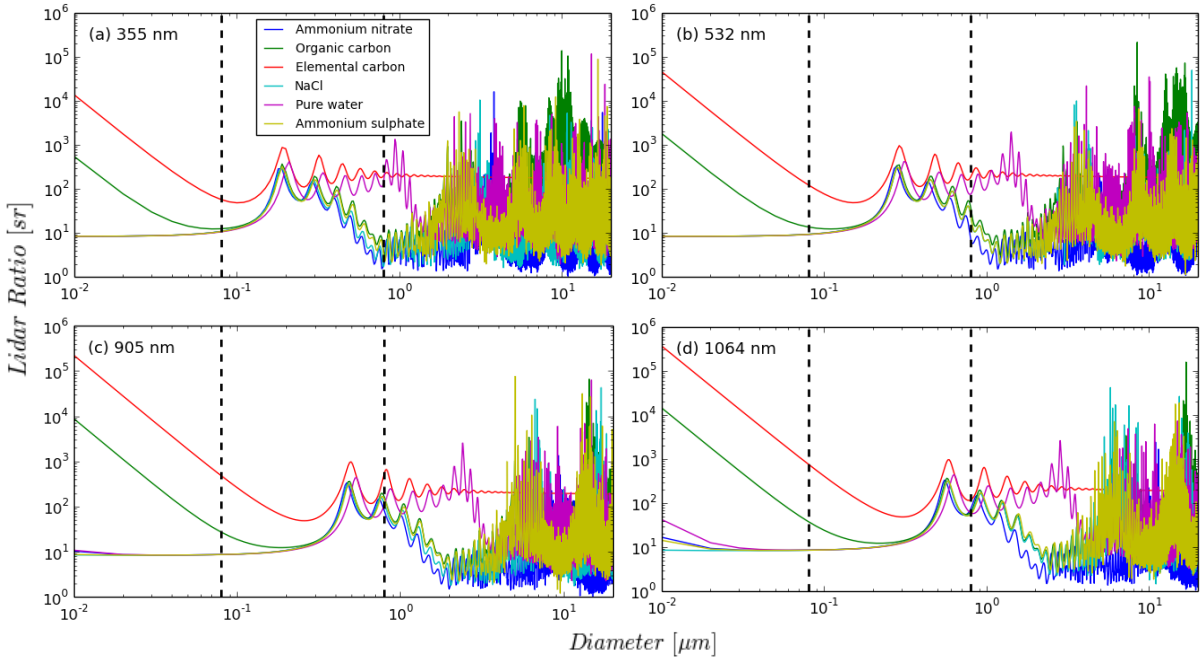

Figure 6: Lidar ratio (S, sr) of pure monodisperse aerosol species for four wavelengths (as Figure 5) using Mie scattering and assuming perfect sphericity. Accumulation diameter range (~80 – 800 nm) indicated (vertical dashed lines) (Figure 1).

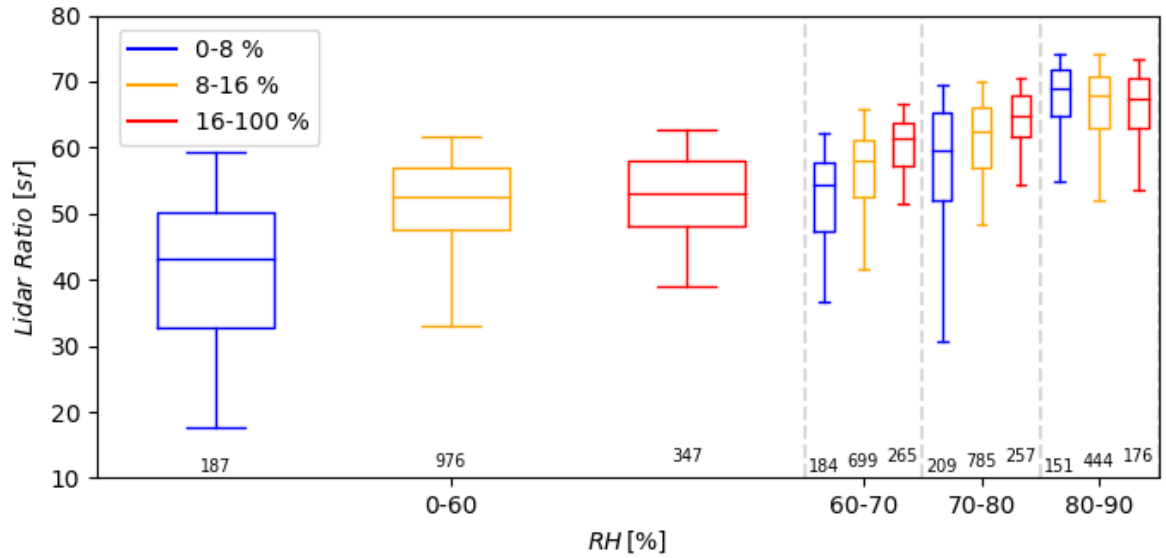

Figure 7: Calculated lidar ratio (S, sr) as Figure 5, but of relative humidity (%, x-axis) then by relative volume of elemental carbon to total aerosol (colour), for 355 nm. Median (box centre line), inter-quartile range (box edges), 5th and 95th percentiles (whiskers). Sample size below each box and whiskers.

Because EC and OC have a relatively high absorption of radiation compared to other ambient aerosols, their presence impacts the bulk aerosol absorption (Esteve et al., 2014). However, the imaginary component of the complex index of refraction (CIR) of these species (which governs absorption), as well as the physical growth factor of OC (g_{OC}) from the absorption of water are relatively uncertain because of the large number of chemical species present and the extent of external mixing (Esteve et al., 2014). Measurements in areas with distinct aerosol sources (e.g. South American biomass burning (Kotchenruther and Hobbs, 1998; Figure 3 in Thornhill et al., 2018), biogenic sources in North America, (Lowenthal et al., 2009; Taylor et al., 2017)) highlight the vast uncertainty in g_{OC}. Observed water soluble fractions of OC vary with location, between 20 and 65% of total OC (Du et al., 2014; Miyazaki et al., 2006; Sullivan et al., 2004; Zappoli et al., 1999) indicating the hygroscopicity of total OC. Uncertainty in g_{OC} arises at NK as the OC sources differ from previous g_{OC} studies, with urban contributions from cooking and fuel burning, and local vegetation differences. To explore the impact of CIR and g_{OC} uncertainty on S variability, five combinations of variables at 905 nm are used (Table 5). For experiment 5, an adjusted g_{OC} (growth is ~1/3 of fresh OC, model 2 in Kotchenruther and Hobbs (1998) hereafter KH98) gives the scattering enhancement factor closest to the literature.

Table 5: Experiment (ID) settings for calculation of lidar ratio S: physical growth factor (g_{OC}) and imaginary component of the complex index of refraction (CIR) for organic carbon (OC) and elemental carbon (EC). Settings modified from default (shaded). Aged and fresh OC growth factors as per Met Office CLASSIC aerosol scheme (Bellouin et al., 2011). KH98 (Kotchenruther and Hobbs 1998) adjusted growth factor best reproduced the scattering enhancement observed. All values applicable for 905 nm. ID= 0 is control (section 3.2).

ID	Physical growth factor (g_{OC})	CIR imaginary component	
Species	*OC*	*OC*	*EC*
0	Aged	0.006	0.700
1	Aged	0.006	0.440
2	Aged	0.010	0.700
3	Aged	0.000	0.700
4	Fresh	0.000	0.700
5	KH98 adjusted	0.006	0.700

The positive *RH - S* relation occurs in all experiments (not shown) with the range of S mostly unchanged. Sensitivity analyses suggest that the uncertainty of the imaginary component of CIR for OC and EC is small when estimating S at NK. Using either fresh or aged OC growth factor has a minor impact. Using KH98 adjusted g_{OC} reduced the inter-quartile range (IQR) and the mean S (30.1 sr, not shown). Hence, constraining g_{OC} uncertainty is expected to reduce the lidar ratio uncertainty. This is in agreement with Esteve et al. (2014) who found the physical growth factor of OC to be important for the calculation of the bulk aerosol optical properties. However, their results also indicate that the uncertainty of the imaginary component of CIR should be accounted for, which is not considered critical in the current analysis.

3.2 Improvement to forward-modelled attenuated backscatter using observed aerosol characteristics

Multiple aerFO experiments are conducted with different combinations of aerosol observations to identify which aerosol characteristics are most important for estimating β_m (section 2.4). Estimates of β_m are compared with observed β_o and summary statistics across all the experiments are shown in Table 6. Statistics computed include the Spearman rank correlation (R_S) and Pearson correlation (R_P) between β_m and β_o, as well as a normalised standard deviation (nSD = $SD(\beta_m)/SD(\beta_o)$). β_m is most relevant for the near surface (height level of *in-situ* aerosol measurements), whereas β_o was taken at 20 m above ground level (section 2.1).

In the control experiment (ID = 0), PM_{10} is the aerosol mass m, used to parameterise N and r_{md}. Modelled and observed attenuated backscatter are highly correlated with both R_S and R_P (0.78 and 0.74, respectively) and statistically significant (> 99.9 %). However, β_m is generally underestimated with a median bias error (medBE) of ~ - 1.1 $\times 10^{-6}$ sr. nSD is low (0.37, i.e. small modelled standard deviation) as the monotonic function of m (PM_{10}, Figure 8) does not account for the large variance observed.

In experiment 1 (ID = 1) observed aerosol number concentration of the accumulation mode replaces the parameterised N, bringing a slight reduction in error. The parameterised aerosol number concentration has slightly underestimated N when $m > \sim 20$ µg kg^{-1} compared to a locally weighted scatter smoothing function (Cleveland, 1979) through N observations (Figure 8a, black (parameterisation) and red (LOWESS) lines). Providing more variable and realistic values of N enhances the modelled variability and increases nSD to 0.68.

For experiment 2, observed dry mean volume radius replaces the parameterised r_{md} causing poorer (cf. ID = 1) correlation coefficients R_S and R_P. Experiment 2 has the lowest nSD (0.32) of all the experiments despite introduced observed variability in r_{md} (Figure 8b). These results suggest the variance of β is controlled more

by the variation in aerosol number concentrations in the accumulation mode than by variation of r_{md} at NK. Hence, a more realistic estimate of N is more beneficial to accurately reproducing β_m than adjusting r_{md}. Overall, underestimation of β_m is greater for experiment 2 (cf. ID = 1). This is likely explained by underestimation of N by aerFO for $m > \sim 20$ µg kg^{-1} (Figure 8a).

Experiment 3, with both observed N and r_{md} for the accumulation mode used, still has a negative medBE (~ - 1.1 ×10^{-6} sr). This suggests other characteristics are important to accurately obtain β_m.

In experiment 4, the N and r_{md} observations used are for both fine and accumulation modes. This addition of fine aerosol mode information has little impact on the results as R_S, R_P, medBE and nSD only differ slightly (cf. ID = 3). This is explained by the impact of aerosol size and surface area on extinction. Given $r_{md} \propto Q_{ext,dry} \propto \sigma_{ext}$, and the average r_{md} of the accumulation mode (0.142 µm) distinctly exceeds that of the fine mode (0.029 µm) by definition, the extinction coefficient (σ_{ext}) of the fine mode is ~100 times smaller than that of the accumulation mode at a wavelength of 905 nm. Although more smaller particles are present, and both N and $f_{ext,rh}(r_{md})$ are greater for the fine mode, the effect of number concentration does not outweigh the size and surface area effects. Hence, we conclude that representing the fine mode N and r_{md} is not critical to accurately estimating β_m at the 905 nm wavelength.

For experiment 5, when N and r_{md} observations for three aerosol modes (fine, accumulation and coarse) are used, β_m is overestimated (medBE ~3.6 ×10^{-7} sr). This demonstrates the strong impact of coarse mode particles (D_v: > 0.8 µm) on the bulk optical properties. The underestimation in experiments 0 - 4 is likely caused by the lack of coarse mode aerosol information (cf. medBE ~-1.1 ×10^{-6} sr (ID = 3, 4)). This is likely to be more important at ~900 nm than 300 – 500 nm.

A strong horizontal advection event likely affects this positive bias. On 04/06/2015 a change in wind direction (not shown) is associated with advection of $(NH_4)_2SO_4$ and NH_4NO_3, leading to a 3 – 4-fold increase in NH_4 of mass and a 2 – 3 increase in NO_3 and SO_4. This impacts the five hours after the air mass change with a larger nSD (2.1). The assumption, all available NH_4 combining with SO_4 and NO_3 when estimating S (section 2.1), might not hold during this period causing the relative amount of $(NH_4)_2SO_4$ and NH_4NO_3 to be overestimated. The associated increase of $f_{ext,rh}$ would explain some of the overestimation of β_m. Removing the affected period (5 hours) reduces the nSD to 1.56. The medBE also improves from 3.6 ×10^{-7} to 2.8 ×10^{-7} sr.

Experiment 6 uses hourly estimates of $Q_{ext,dry}$ and $f_{ext,rh}$ to replace the monthly LUT. The medBE, nSD and correlation statistics are similar to experiment 5. As additional relative mass of different aerosol species information does not improve β_m, the default monthly LUT of $Q_{ext,dry}$ and $f_{ext,rh}$ appear adequate. However, other uncertainties within aerFO may limit its ability to improve β_m. For instance, assuming particles are perfectly spherical when using Mie theory will introduce errors. As particles likely interact and aggregate, their interaction with water and light is altered. Hence, not considering internal mixing in aerFO or its LUT, is another source of uncertainty. Measurement uncertainties arise in β_o from imperfect overlap correction and calibration. Height differences between the near-surface *in-situ* aerosol observations and ceilometer β_o also cause uncertainties.

Finally, experiment 7 uses hourly S estimates (section 3.1) to ID=6. The error is greater than experiments 5 and 6 with a larger standard deviation and interquartile range in $\beta_m - \beta_o$. Correlations between model results and observations (R_S and R_P) are the lowest across all experiments. The large differences between β_m and β_o is reflected in a high nSD (3.5) but excluding the five hours (see experiment 5 discussion) reduces nSD to 1.83. The reduced overall performance of experiment 7 suggests the method to compute S (section 3.1) is unable to provide hourly variability. Specifically, uncertainties in estimating S (section 3.1) are likely varying with aerosol as particles interact and age, including through hysteresis, relative aerosol speciation across the size distribution, as well as OC and EC characteristics. Hence, the method is currently limited to providing only the overall behaviour of the lidar ratio.

Table 6: aerFO model estimates for experiments (ID) with different aerosol observations (Table 4), observed attenuated backscatter and $\beta_m - \beta_o$ evaluation statistics. Metrics: standard deviation (SD), interquartile range (IQR), normalised standard deviation (nSD = SD(β_m)/ SD(β_o)), Spearman rank (R_S) and Pearson (R_P) correlation between β_m and β_o. All correlation coefficients are statistically significant (> 99.9 %). Equal sample size of 106 hours from the seven days for all experiments.

		ID							
		0	1	2	3	4	5	6	7
β_m	Mean	5.6×10^{-7}	7.8×10^{-7}	4.6×10^{-7}	6.2×10^{-7}	6.3×10^{-7}	2.4×10^{-6}	2.4×10^{-6}	3.0×10^{-6}
	Median	5.3×10^{-7}	7.0×10^{-7}	4.6×10^{-7}	5.4×10^{-7}	5.4×10^{-7}	2.1×10^{-6}	2.1×10^{-6}	2.6×10^{-6}
β_o	Mean	1.8×10^{-6}							
	Median	1.6×10^{-6}							
$\beta_m - \beta_o$	Mean	-1.3×10^{-6}	-1.1×10^{-6}	-1.4×10^{-6}	-1.2×10^{-6}	-1.2×10^{-6}	5.3×10^{-6}	5.3×10^{-6}	1.1×10^{-6}
	Median	-1.1×10^{-6}	-1.1×10^{-6}	-1.2×10^{-6}	-1.1×10^{-6}	-1.1×10^{-6}	3.6×10^{-7}	4.0×10^{-7}	8.2×10^{-7}
	SD	4.7×10^{-7}	4.1×10^{-7}	5.2×10^{-7}	4.3×10^{-7}	4.3×10^{-7}	9.6×10^{-7}	9.3×10^{-7}	1.9×10^{-6}
	IQR	5.9×10^{-7}	5.1×10^{-7}	6.5×10^{-7}	6.6×10^{-7}	6.5×10^{-7}	1.1×10^{-6}	9.7×10^{-7}	9.7×10^{-7}
nSD		0.37	0.68	0.32	0.50	0.51	2.14	2.14	3.48
R_S		0.78	0.68	0.66	0.70	0.70	0.72	0.72	0.47
R_P		0.78	0.74	0.62	0.75	0.75	0.74	0.76	0.50

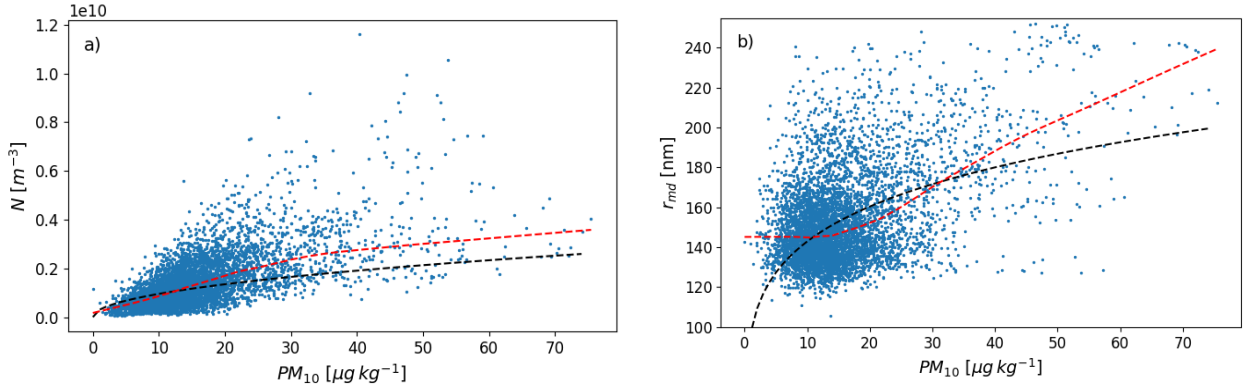

Figure 8: Hourly observations for two years (2014 – 2015) at NK (Figure 1) of PM_{10} concentrations and aerosol characteristics for the accumulation diameter range (80 – 800 nm): a) total particle number concentration (N) and b) dry volume mean radius (r_{md}) with a locally weighted scatterplot smoothing function (LOWESS, red). The aerFO parameterisations (black) are a function of aerosol mass (m) derived from PM_{10} concentration.

4 Conclusions

The Warren et al. (2018) aerosol forward operator (aerFO) is used to quantify the relative importance of accurately describing different aerosol characteristics

when estimating attenuated backscatter (β_m) at an urban background site. Observations are used to calculate aerosol variables by aerFO in increasing detail, including total aerosol mass, number concentration and mean volume radius for fine, accumulation and coarse modes. Results inform the development of the Met Office MURK visibility scheme for application in urban settings, as the aerFO links the output of this scheme to observed aerosol characteristics.

aerFO is used to assess the relative importance of various aerosol characteristics when modelling aerosol optical properties an urban background site in London, UK. It is concluded that:

- Monotonic parameterisations within aerFO for total particle number concentration and dry volume mean radius from aerosol mass alone lead to an underestimation of the variance of attenuated backscatter by about 2/3.
- A more realistic representation of total particle number concentration is the most critical factor for estimating accurate attenuated backscatter and should be considered a priority in future developments of Met Office NWP aerosol schemes for estimating aerosol optical properties.
- Using more realistic values of dry volume mean radius has little effect.
- Improving the representation of aerosol physical characteristics in the accumulation and coarse mode will likely lead to better model performance:
    - Providing a more realistic estimate of the total particle number concentration for the accumulation mode (diameter: 0.08 – 0.8 μm) based on observations improves the modelled variability.
    - More realistic coarse mode (diameter: > 0.8 μm) aerosol information leads to a clear increase in β_m bringing the model results closer to the observations and reducing the mean bias error by 69.1 %. Hence, this aspect bears potential for the improvement of the Met Office MURK aerosol scheme.
    - aerFO needs to represent the coarse mode in addition to the accumulation mode to better estimate the magnitude of β_m.
- At a wavelength of 905 nm the extinction coefficient of the fine mode aerosol (diameter: < 0.08 μm) is ~100 times smaller than that of the accumulation mode, so that more realistic fine mode information has no clear benefit.
- Constraining aerosol species relative mass has little impact on modelled results, however, this may be attributed to a limitation of the aerFO which does not account for internal mixing but rather used some simplifications with respect to aerosol hygroscopic and optical properties.

A new method to estimate the lidar ratio (*S*) from observations is developed that uses relative humidity and *in-situ* aerosol observations. This extends the possibility to calculate the lidar ratio without the need for the rare measurements from Raman lidars or sunphotometers. S can be used to derive further aerosol optical properties (e.g. optical depth, extinction) from elastic-backscatter lidars (e.g. ceilometers), and the ratio can be parameterised before use in forward models, to minimise computational expense. For the London background site, modelled *S* varies with wavelength between 14 – 80 sr across four common lidar wavelengths (355, 532, 905 and 1064 nm), values consistent with the literature. A strong dependence of the lidar ratio on relative humidity is found which varies between common lidar wavelengths; a relation not found in the wider literature. The relation found is due to another relation between lidar wavelength and aerosol size.

Adequately representing elemental carbon (EC) is important when estimating *S* at shorter wavelengths (355 and 532 nm) and low relative humidity, given its characteristically high absorption of radiation. The effect of hygroscopic aerosol swelling likely explains why EC is less important at longer wavelengths and at higher relative humidity. Remaining uncertainties when estimating *S* are associated with the assumption of particle sphericity for use with Mie theory, the speciation of the number distribution, and not including the effect of internal aerosol mixing which would lead to errors in the hygroscopic growth of particles, including hysteresis effects. These uncertainties could not be constrained in the current study due to a lack of appropriate observations. As here only the near surface variability of *S* is estimated from aerosol and relative humidity variations, future work should investigate how the input variables vary with height and if near surface *S* estimates could be applied to full vertical profiles of β_m.

The current study uses a range of very detailed aerosol observations. However, data availability of number concentrations is slightly limited for relatively large particles (here > 0.6 μm). While small particles are a critical research topic given their impact on health, the fundamental impact of larger particles on bulk optical characteristics of aerosols warrant additional, increased and simultaneous monitoring of number concentrations in both the accumulation and the coarse mode. Furthermore, to estimate optical properties at more and diverse locations, more observation of speciated aerosol mass alongside number size distributions are needed.

5 Acknowledgements

EW was funded by the NERC Scenario DTP and University of Reading. The instruments and measurements have been funded and operated by LUMO (NERC ClearfLo, NERC TRUC, EPSRC DARE, KCL, UoR, Newton Fund/Met Office CSSP China (SG, SK), EUf7 BRIDGE, EUf7 emBRACE, H2020 UrbanFluxes), LAQN/ERG, MO, DEFRA, STFC, NPL; Paul Quincy, Jordan Tompkins, James Allen, Max Priestman, Anke Finnenkoetter, Adrian Hill, Jordan Tompkins, Paul Agnew, Emma Hopkin, Anthony Illingworth and Helen Dacre; and the vast number of people who help keep the equipment operating on a daily basis. We acknowledge the contribution of one of the authors, Sue Ballard, who sadly passed away before the completion of this paper.

6 References

Abdalmogith, S.S., Harrison, R.M., 2006. An analysis of spatial and temporal properties of daily sulfate, nitrate and chloride concentrations at UK urban and rural sites. J. Environ. Monit. 8, 691–699. https://doi.org/10.1039/b601562j

Abdalmogith, S.S., Harrison, R.M., 2005. The use of trajectory cluster analysis to examine the long-range transport of secondary inorganic aerosol in the UK. Atmos. Environ. 39, 6686–6695. https://doi.org/10.1016/j.atmosenv.2005.07.059

Barnaba, F., Tafuro, A.M., De Tomasi, F., Perrone, M.R., 2007. Observed and simulated vertically resolved optical properties of continental aerosols over southeastern Italy: A closure study. J. Geophys. Res. Atmos. 112, 1–16. https://doi.org/10.1029/2006JD007926

Beccaceci, S., Mustoe, C., Butterfield, D., Tompkins, J., Sarantaridis, D., P., Q., Brown, R., Green, D., Fuller, G., Tremper, A., Font Font, A., Jones, A., 2013. Airborne Particulate Concentrations and Numbers in the United Kingdom (phase 3) - Annual report 2012. Teddington, U.K.

Bellouin, N., Rae, J., Jones, A., Johnson, C., Haywood, J., Boucher, O., 2011. Aerosol forcing in the Climate Model Intercomparison Project (CMIP5) simulations by HadGEM2-ES and the role of ammonium nitrate. J. Geophys. Res. Atmos. 116, 1–25. https://doi.org/10.1029/2011JD016074

Benedetti, A., Dabas, A., 2016. Assessment of the necessary developments to assimilate Aeolus and EarthCARE aerosol profile products, Technical Note 1 of ESA contract number 4000116106.

Benedetti, A., Morcrette, J.-J., Boucher, O., Dethof, A., Engelen, R.J., Fisher, M., Flentje, H., Huneeus, N., Jones, L., Kaiser, J.W., Kinne, S., Mangold, A., Razinger, M., Simmons, A.J., Suttie, M., 2009. Aerosol analysis and forecast in the European Centre for Medium-Range Weather Forecasts Integrated Forecast System: 2. Data assimilation. J. Geophys. Res. 114, D13205. https://doi.org/10.1029/2008JD011115

Briggs, N.L., Long, C.M., 2016. Critical review of black carbon and elemental carbon source apportionment in Europe and the United States. Atmos. Environ. 144, 409–427. https://doi.org/10.1016/j.atmosenv.2016.09.002

Burton, S.P., Ferrare, R.A., Hostetler, C.A., Hair, J.W., Rogers, R.R., Obland, M.D., Butler, C.F., Cook, A.L., Harper, D.B., Froyd, K.D., 2012. Aerosol classification using airborne High Spectral Resolution Lidar measurements-methodology and examples. Atmos. Meas. Tech. 5, 73–98. https://doi.org/10.5194/amt-5-73-2012

Cattrall, C., Reagan, J., Thome, K., Dubovik, O., 2005. Variability of aerosol and spectral lidar and backscatter and extinction ratios of key aerosol types derived from selected Aerosol Robotic Network locations. J. Geophys. Res. D Atmos. 110, 1–13. https://doi.org/10.1029/2004JD005124

Cavalli, F., Viana, M., Yttri, K.E., Genberg, J., Putaud, J.-P., 2010. Toward a standardised thermal-optical protocol for measuring atmospheric organic and elemental carbon: the EUSAAR protocol. Atmos. Meas. Tech. 3, 79–89. https://doi.org/10.5194/amt-3-79-2010

Chan, K.L., Wiegner, M., Flentje, H., Mattis, I., Wagner, F., Gasteiger, J., Geiß, A., 2018. Evaluation of ECMWF-IFS (version 41R1) operational model forecasts of aerosol transport by using ceilometer network measurements. Geosci. Model Dev. 11, 3807–3831. https://doi.org/10.5194/gmd-11-3807-2018

Charlton-Perez, C., Simonin, D., Ballard, S., Hopkin, E., Illingworth, A., Kotthaus, S., Westbrook, C., Grimmond, C.S.B., 2016. Suitability of Ceilometer Observations for DA, Data Assimilation and Ensembles Science Report 10. Met Office.

Clark, P.A., Harcourt, S.A., Macpherson, B., Mathison, C.T., Cusack, S., Naylor, M., 2008. Prediction of visibility and aerosol within the operational Met Office Unified Model. I: Model formulation and variational assimilation. Q. J. R. Meteorol. Soc. 134, 1801–1816. https://doi.org/10.1002/qj.318

Cleveland, W.S., 1979. Robust Locally Weighted Regression and Smoothing Scatterplots. J. Am. Stat. Assoc. 74, 829. https://doi.org/10.2307/2286407

Crilley, L.R., Lucarelli, F., Bloss, W.J., Harrison, R.M., Beddows, D.C., Calzolai, G., Nava, S., Valli, G., Bernardoni, V., Vecchi, R., 2017. Source apportionment of fine and coarse particles at a roadside and urban background site in London during the 2012 summer ClearfLo campaign. Environ. Pollut. 220, 766–778. https://doi.org/10.1016/j.envpol.2016.06.002

DeCarlo, P.F., Slowik, J.G., Worsnop, D.R., Davidovits, P., Jimenez, J.L., 2004. Particle Morphology and Density Characterization by Combined Mobility and Aerodynamic Diameter Measurements. Part 1: Theory. Aerosol Sci. Technol. 38, 1185–1205. https://doi.org/10.1080/027868290903907

DEFRA, 2018a. Site Information for London N. Kensington (UKA00253) [WWW Document]. URL https://uk-air.defra.gov.uk/networks/site-info?site_id=KC1#startcontent (accessed 10.8.18).

DEFRA, 2018b. Particle Numbers and Concentrations Network [WWW Document]. URL https://uk-air.defra.gov.uk/networks/network-info?view=particle (accessed 10.8.18).

Dionisi, D., Barnaba, F., Diémoz, H., Di Liberto, L., Gobbi, G.P., 2018. A multi-wavelength numerical model in support to quantitative retrievals of aerosol properties from automated-lidar-ceilometers and test applications for AOT and PM10 estimation. Atmos. Meas. Tech. Discuss. 1–47. https://doi.org/10.5194/amt-2018-79

Doherty, S.J., Anderson, T.L., Charlson, R.J., 1999. Measurement of the lidar ratio for atmospheric aerosols with a 180° backscatter nephelometer. Appl. Opt. 38, 1823. https://doi.org/10.1364/AO.38.001823

Du, Z., He, K., Cheng, Y., Duan, F., Ma, Y., Liu, J., Zhang, X., Zheng, M., Weber, R., 2014. A yearlong study of water-soluble organic carbon in Beijing I: Sources and its primary vs. secondary nature. Atmos. Environ. 92, 514–521. https://doi.org/10.1016/j.atmosenv.2014.04.060

Dubovik, O., King, M.D., 2000. A flexible inversion algorithm for retrieval of aerosol optical properties from Sun and sky radiance measurements. J. Geophys. Res. Atmos. 105, 20673–20696. https://doi.org/10.1029/2000JD900282

ECMWF, 2018. Operational configurations of the ECMWF Integrated Forecasting System (IFS) [WWW Document]. URL https://www.ecmwf.int/en/forecasts/documentation-and-support (accessed 12.18.18).

Esteve, A.R., Highwood, E.J., Morgan, W.T., Allen, G., Coe, H., Grainger, R.G., Brown, P., Szpek, K., 2014. A study on the sensitivities of simulated aerosol optical properties to composition and size distribution using airborne measurements. Atmos. Environ. 89, 517–524. https://doi.org/10.1016/j.atmosenv.2014.02.063

Fernald, F.G., 1984. Analysis of atmospheric lidar observations: some comments. Appl. Opt. 23, 652. https://doi.org/10.1364/AO.23.000652

Fierz-Schmidhauser, R., Zieger, P., Wehrle, G., Jefferson, A., Ogren, J.A., Baltensperger, U., Weingartner, E., 2010. Measurement of relative humidity dependent light scattering of aerosols. Atmos. Meas. Tech. 3, 39–50. https://doi.org/10.5194/amt-3-39-2010

Fitzgerald, J.W., 1975. Approximation Formulas for the Equilibrium Size of an Aerosol Particle as a Function of Its Dry Size and Composition and the Ambient Relative Humidity. J. Appl. Meteorol. 14, 1044–1049. https://doi.org/10.1175/1520-0450(1975)014<1044:AFFTES>2.0.CO;2

Flentje, H., Heese, B., Reichardt, J., Thomas, W., 2010. Aerosol profiling using the ceilometer network of the German Meteorological Service. Atmos. Meas. Tech. Discuss. 3, 3643–3673. https://doi.org/10.5194/amtd-3-3643-2010

Geisinger, A., Behrendt, A., Wulfmeyer, V., Strohbach, J., Förstner, J., Potthast, R., 2017. Development and application of a backscatter lidar forward operator for quantitative validation of aerosol dispersion models and future data assimilation. Atmos. Meas. Tech. 10, 4705–4726. https://doi.org/10.5194/amt-10-4705-2017

Haeffelin, M., Laffineur, Q., Bravo-Aranda, J.A., Drouin, M.A., Casquero-Vera, J.A., Dupont, J.C., De Backer, H., 2016. Radiation fog formation alerts using attenuated backscatter power from automatic lidars and ceilometers. Atmos. Meas. Tech. 9, 5347–5365. https://doi.org/10.5194/amt-9-5347-2016

Hair, J.W., Hostetler, C.A., Cook, A.L., Harper, D.B., Ferrare, R.A., Mack, T.L., Welch, W., Izquierdo, L.R., Hovis, F.E., 2008. Airborne High Spectral Resolution Lidar for profiling aerosol optical properties. Appl. Opt. 47, 6734. https://doi.org/10.1364/AO.47.006734

Hama, S.M.L., Cordell, R.L., Kos, G.P.A., Weijers, E.P., Monks, P.S., 2017a. Sub-micron particle number size distribution characteristics at two urban locations in Leicester. Atmos. Res. 194, 1–16. https://doi.org/10.1016/j.atmosres.2017.04.021

Hama, S.M.L., Cordell, R.L., Monks, P.S., 2017b. Quantifying primary and secondary source contributions to ultrafine particles in the UK urban background. Atmos. Environ. 166, 62–78. https://doi.org/10.1016/j.atmosenv.2017.07.013

Harrison, R.M., Dall'Osto, M., Beddows, D.C.S., Thorpe, A.J., Bloss, W.J., Allan, J.D., Coe, H., Dorsey, J.R., Gallagher, M., Martin, C., Whitehead, J., Williams, P.I., Jones, R.L., Langridge, J.M., Benton, A.K., Ball, S.M., Langford, B., Hewitt, C.N., Davison, B., Martin, D., Petersson, K.F., Henshaw, S.J., White, I.R., Shallcross, D.E., Barlow, J.F., Dunbar, T., Davies, F., Nemitz, E., Phillips, G.J., Helfter, C., Di Marco, C.F., Smith, S., 2012. Atmospheric chemistry and physics in the atmosphere of a developed megacity (London): An overview of the REPARTEE experiment and its conclusions. Atmos. Chem. Phys. 12, 3065–3114. https://doi.org/10.5194/acp-12-3065-2012

Heese, B., Flentje, H., Althausen, D., Ansmann, A., Frey, S., 2010. Ceilometer lidar comparison: Backscatter coefficient retrieval and signal-to-noise ratio determination. Atmos. Meas. Tech. 3, 1763–1770. https://doi.org/10.5194/amt-3-1763-2010

Hinds, W.C., 1999. Aerosol Technology: Properties, Behaviour and Measurement of Airborne Particles. Wiley, New York, USA.

Hofman, J., Staelens, J., Cordell, R., Stroobants, C., Zikova, N., Hama, S.M.L., Wyche, K.P., Kos, G.P.A., Van Der Zee, S., Smallbone, K.L., Weijers, E.P., Monks, P.S., Roekens, E., 2016. Ultrafine particles in four European urban environments: Results from a new continuous long-term monitoring network. Atmos. Environ. 136, 68–81. https://doi.org/10.1016/j.atmosenv.2016.04.010

Hopkin, E., Illingworth, A., Charlton-Perez, C., Westbrook, C., Ballard, S., 2019. A robust automated technique for operational calibration of ceilometers using integrated backscatter from totally attenuating liquid cloud. Atmos. Meas. Tech. Discuss. https://doi.org/10.5194/amt-2018-427

Illingworth, A.J., Hogan, R.J., O'Connor, E.J., Bouniol, D., Brooks, M.E., Delanoë, J., Donovan, D.P., Eastment, J.D., Gaussiat, N., Goddard, J.W.F., Haeffelin, M., Klein Baltinik, H., Krasnov, O.A., Pelon, J., Piriou, J.M., Protat, A., Russchenberg, H.W.J., Seifert, A., Tompkins, A.M., van Zadelhoff, G.J., Vinit, F., Willen, U., Wilson, D.R., Wrench, C.L., 2007. Cloudnet: Continuous evaluation of cloud profiles in seven operational models using ground-based observations. Bull. Am. Meteorol. Soc. 88, 883–898. https://doi.org/10.1175/BAMS-88-6-883

Jacobson, M.Z., 2005. Fundamentals of Atmospheric Modeling, 2nd Editio. ed. Cambridge University Press, Cambridge, UK.

Klett, J.D., 1981. Stable analytical inversion solution for processing lidar returns. Appl. Opt. 20, 211–220. https://doi.org/10.1364/AO.20.000211

Klompmaker, J.O., Montagne, D.R., Meliefste, K., Hoek, G., Brunekreef, B., 2015. Spatial variation of ultrafine particles and black carbon in two cities: Results from a short-term measurement campaign. Sci. Total Environ. 508, 266–275. https://doi.org/10.1016/j.scitotenv.2014.11.088

Kotchenruther, R.A., Hobbs, P. V, 1998. Humidification factors of aerosols from biomass burning in Brazil. J. Geophys. Res. Atmos. 103, 32081–32089. https://doi.org/10.1029/98JD00340

Kotthaus, S., Grimmond, C.S.B., 2018. Atmospheric boundary-layer characteristics from ceilometer measurements. Part 2: Application to London's urban boundary layer. Q. J. R. Meteorol. Soc. 144, 1511–1524. https://doi.org/10.1002/qj.3298

Kotthaus, S., Grimmond, C.S.B., 2014. Energy exchange in a dense urban environment – Part I: Temporal variability of long-term observations in central London. Urban Clim. 10, 261–280. https://doi.org/10.1016/j.uclim.2013.10.002

Kotthaus, S., Halios, C.H., Barlow, J.F., Grimmond, C.S.B., 2018. Volume for pollution dispersion: London's atmospheric boundary layer during ClearfLo observed with two ground-based lidar types. Atmos. Environ. 190, 401–414. https://doi.org/10.1016/j.atmosenv.2018.06.042

Kotthaus, S., O'Connor, E., Münkel, C., Charlton-Perez, C., Haeffelin, M., Gabey, A.M., Grimmond, C.S.B., 2016. Recommendations for processing atmospheric attenuated backscatter profiles from Vaisala CL31 ceilometers. Atmos. Meas. Tech. 9, 3769–3791. https://doi.org/10.5194/amt-9-3769-2016

Li, Jian, Li, C., Zhao, Y., Li, Jing, Chu, Y., 2016. Geometrical constraint experimental determination of Raman lidar overlap profile. Appl. Opt. 55, 4924–4928. https://doi.org/http://dx.doi.org/10.1364/AO.55.004924 1.

Liu, D., Allan, J.D., Young, D.E., Coe, H., Beddows, D., Fleming, Z.L., Flynn, M.J., Gallagher, M.W., Harrison, R.M., Lee, J., Prevot, A.S.H., Taylor, J.W., Yin, J., Williams, P.I., Zotter, P., 2014. Size distribution, mixing state and source apportionment of black carbon aerosol in London during winter time. Atmos. Chem. Phys. 14, 10061–10084. https://doi.org/10.5194/acp-14-10061-2014

Liu, Y., Daum, P.H., 2008. Relationship of refractive index to mass density and self-consistency of mixing rules for multicomponent mixtures like ambient aerosols. J. Aerosol Sci. 39, 974–986. https://doi.org/10.1016/j.jaerosci.2008.06.006

Lowenthal, D., Zielinska, B., Mason, B., Samy, S., Samburova, V., Collins, D., Spencer, C., Taylor, N., Allen, J., Kumar, N., 2009. Aerosol characterization

studies at Great Smoky Mountains National Park, summer 2006. J. Geophys. Res. Atmos. 114, 1–11. https://doi.org/10.1029/2008JD011274
Madonna, F., Amato, F., Vande Hey, J., Pappalardo, G., 2014. Ceilometer aerosol profiling vs. Raman lidar in the frame of INTERACT campaign of ACTRIS. Atmos. Meas. Tech. Discuss. 7, 12407–12447. https://doi.org/10.5194/amtd-7-12407-2014
Madonna, F., Rosoldi, M., Lolli, S., Amato, F., Vande Hey, J., Dhillon, R., Zheng, Y., Brettle, M., Pappalardo, G., 2018. Intercomparison of aerosol measurements performed with multi-wavelength Raman lidars, automatic lidars and ceilometers in the framework of INTERACT-II campaign. Atmos. Meas. Tech. 11, 2459–2475. https://doi.org/10.5194/amt-11-2459-2018
Manners, J., Edwards, J.M., Hill, P., Thelen, J., 2015. SOCRATES Technical Guide Suite Of Community Radiative Transfer codes based on Edwards and Slingo. Exeter, UK.
Martin, G.M., Ringer, M.A., Pope, V.D., Jones, A., Dearden, C., Hinton, T.J., 2006. The physical properties of the atmosphere in the new Hadley Centre Global Environmental Model (HadGEM1). Part I: Model description and global climatology. J. Clim. 19, 1274–1301. https://doi.org/10.1175/jcli3636.1
Met Office, 2017. LIDARNET- LCBR Network Backscatter visualisation [WWW Document]. URL https://www.metoffice.gov.uk/public/lidarnet/lcbr-network.html (accessed 10.25.17).
Mittal, L., Baker, T., Fuller, G., 2016. London Air Quality Network Summary Report 2014. Kings College London, London, UK.
Miyazaki, Y., Kondo, Y., Takegawa, N., Komazaki, Y., Fukuda, M., Kawamura, K., Mochida, M., Okuzawa, K., Weber, R.J., 2006. Time-resolved measurements of water-soluble organic carbon in Tokyo. J. Geophys. Res. Atmos. 111. https://doi.org/10.1029/2006JD007125
Muller, C.L., Chapman, L., Grimmond, C.S.B., Young, D.T., Cai, X.-M., 2013. Toward a Standardized Metadata Protocol for Urban Meteorological Networks. Bull. Am. Meteorol. Soc. 94, 1161–1185. https://doi.org/10.1175/BAMS-D-12-00096.1
Müller, D., Ansmann, A., Mattis, I., Tesche, M., Wandinger, U., Althausen, D., Pisani, G., 2007. Aerosol-type-dependent lidar ratios observed with Raman lidar. J. Geophys. Res. Atmos. 112, 1–11. https://doi.org/10.1029/2006JD008292
Münkel, C., Emeis, S., Müller, W.J., Schaefer, K.P., 2004. Aerosol concentration measurements with a lidar ceilometer: results of a one year measuring campaign. Proc. SPIE--the Int. Soc. Opt. Eng. 5235, 486–496. https://doi.org/10.1117/12.511104
O'Connor, E.J., Illingworth, A.J., Hogan, R.J., 2004. A Technique for Autocalibration of Cloud Lidar. Am. Meteorol. Soc. 21, 777–786. https://doi.org/10.1175/1520-0426(2004)021<0777:ATFAOC>2.0.CO;2
Osborne, M., Adam, M., Buxmann, J., Sugier, J., Marenco, F., Haywood, J., 2018. Saharan dust and biomass burning aerosols during ex-hurricane Ophelia : validation of the new UK lidar and sun-photometer network.
Papayannis, A., Balis, D., Amiridis, V., Chourdakis, G., Tsaknakis, G., Zerefos, C., Castanho, a. D. a., Nickovic, S., Kazadzis, S., Grabowski, J., 2005. Measurements of Saharan dust aerosols over the Eastern Mediterranean using elastic backscatter-Raman lidar, spectrophotometric and satellite observations in the frame of the EARLINET project. Atmos. Chem. Phys. Discuss. 5, 2075–2110. https://doi.org/10.5194/acpd-5-2075-2005
Pappalardo, G., Amodeo, A., Apituley, A., Comeron, A., Freudenthaler, V., Linné, H., Ansmann, A., Bösenberg, J., D'Amico, G., Mattis, I., Mona, L., Wandinger, U., Amiridis, V., Alados-Arboledas, L., Nicolae, D., Wiegner, M., 2014. EARLINET towards an advanced sustainable European aerosol lidar network. Atmos. Meas. Tech. 7, 2389–2409. https://doi.org/10.5194/amt-7-2389-2014
Reid, J.S., Kuehn, R.E., Holz, R.E., Eloranta, E.W., Kaku, K.C., Kuang, S., Newchurch, M.J., Thompson, A.M., Trepte, C.R., Zhang, J., Atwood, S.A., Hand, J.L., Holben, B.N., Minnis, P., Posselt, D.J., 2017. Ground-based High Spectral Resolution Lidar observation of aerosol vertical distribution in the summertime Southeast United States. J. Geophys. Res. 122, 2970–3004. https://doi.org/10.1002/2016JD025798
Roessler, D.M., Faxvog, F.R., 1981. Visibility in absorbing aerosols. Atmos. Environ. 15, 151–155. https://doi.org/10.1016/0004-6981(81)90006-8
Ruths, M., von Bismarck-Osten, C., Weber, S., 2014. Measuring and modelling the local-scale spatio-temporal variation of urban particle number size distributions and black carbon. Atmos. Environ. 96, 37–49. https://doi.org/10.1016/j.atmosenv.2014.07.020
Schkolnik, G., Chand, D., Hoffer, A., Andreae, M.O., Erlick, C., Swietlicki, E., Rudich, Y., 2007. Constraining the density and complex refractive index of elemental and organic carbon in biomass burning aerosol using optical and chemical measurements. Atmos. Environ. 41, 1107–1118. https://doi.org/10.1016/j.atmosenv.2006.09.035
Seinfeld, J.H., Pandis, S.N., 2016. Atmospheric Chemistry and Physics: From Air Pollution to Climate Change. Wiley, Haboken.
Smith, M.L., Bertram, A.K., Martin, S.T., 2012. Deliquescence, efflorescence, and phase miscibility of mixed particles of ammonium sulfate and isoprene-derived secondary organic material. Atmos. Chem. Phys. 12, 9613–9628. https://doi.org/10.5194/acp-12-9613-2012
Song, X., Zhai, X., Liu, L., Wu, S., 2017. Lidar and Ceilometer Observations and Comparisons of Atmospheric Cloud Structure at Nagqu of Tibetan Plateau in 2014 Summer. Atmosphere (Basel). 8, 9. https://doi.org/10.3390/atmos8010009
Song, Y., Zhang, B., Shi, G., Li, S., Di, H., Yan, Q., Hua, D., 2018. Correlation between the lidar ratio and the Ångström exponent of various aerosol types. Particuology. https://doi.org/10.1016/j.partic.2017.12.002
Stachlewska, I.S., Samson, M., Zawadzka, O., Harenda, K.M., Janicka, L., Poczta, P., Szczepanik, D., Heese, B., Wang, D., Borek, K., Tetoni, E., Proestakis, E., Siomos, N., Nemuc, A., Chojnicki, B.H., Markowicz, K.M., Pietruczuk, A., Szkop, A., Althausen, D., Stebel, K., Schuettemeyer, D., Zehner, C., 2018. Modification of local urban aerosol properties by long-range transport of biomass burning aerosol. Remote Sens. 10, 1–28. https://doi.org/10.3390/rs10030412
Stull, R.B., 1988. An Introduction to Boundary Layer Meteorology. Kluwer Academic Publishers, Dordlecht, Netherlands.
Sullivan, A.P., Weber, R.J., Clements, A.L., Turner, J.R., Bae, M.S., Schauer, J.J., 2004. A method for on-line measurement of water-soluble organic carbon in ambient aerosol particles: Results from an urban site. Geophys. Res. Lett. 31, 14–17. https://doi.org/10.1029/2004GL019681
Tang, I.N., Munkelwitz, H.R., 1994. Water activities, densities, and refractive indicies of aqueous sulfates and sodium nitrate droplets of atmospheric importance. J. Geophys. Res. 99, 18801–18808.
Tang, Y., Lean, H.W., Bornemann, J., 2013. The benefits of the Met Office variable resolution NWP model for forecasting convection. Meteorol. Appl. 20, 417–426. https://doi.org/10.1002/met.1300
Taylor, N.F., Collins, D.R., Lowenthal, D.H., McCubbin, I.B., Gannet Hallar, A., Samburova, V., Zielinska, B., Kumar, N., Mazzoleni, L.R., 2017. Hygroscopic growth of water soluble organic carbon isolated from atmospheric aerosol collected at US national parks and Storm Peak Laboratory. Atmos. Chem. Phys. 17, 2555–2571. https://doi.org/10.5194/acp-17-2555-2017
Thermo Fisher Scientific, 2015. Partisol 2025i Sequential Air Sampler/ Partisol 2025i-D Dichotomous Sequential Air Sampler Instruction Manual [WWW Document]. URL https://assets.thermofisher.com/TFS-Assets/LSG/manuals/EPM-manual-Partisol-2025i-2025iD.pdf (accessed 10.11.18).
Thornhill, G.D., Ryder, C.L., Highwood, E.J., Shaffrey, L.C., Johnson, B.T., 2018. The effect of South American biomass burning aerosol emissions on the regional climate. Atmos. Chem. Phys. 18, 5321–5342. https://doi.org/10.5194/acp-18-5321-2018
TSI, 2009. Series 3080: Electrostatic Classifiers [WWW Document]. URL http://cires1.colorado.edu/jimenez-group/Manuals/SMPS_3080_manual.pdf (accessed 10.10.18).
TSI, 2007. Model 3775 Condensation Particle Counter: Operation and Service Manual [WWW Document]. URL http://dustmonitors.ru/d/68562/d/cpc-3775r.pdf (accessed 10.10.18).
TSI, 2004. Model 3321 Aerodynamic Particle Sizer® Spectrometer: Instruction Manual [WWW Document]. URL http://www.wmo-gaw-wcc-aerosol-physics.org/files/aps_3321.pdf (accessed 10.10.18).
URG, 2011. Ambient Ion Monitor: Operation Manual URG-9000B [WWW Document]. URL http://www.urgcorp.com/testupdate/library/manuals/URG-9000B Operations Manual.pdf (accessed 10.11.18).
Varutbangkul, V., Brechtel, F.J., Bahreini, R., Ng, N.L., Keywood, M.D., Kroll, J.H., Flagan, R.C., Seinfeld, J.H., Lee, a., Goldstein, a. H., 2006. Hygroscopicity of secondary organic aerosols formed by oxidation of cycloalkenes, monoterpenes, sesquiterpenes, and related compounds. Atmos. Chem. Phys. Discuss. 6, 1121–1177. https://doi.org/10.5194/acpd-6-1121-2006
Wagner, P., Schäfer, K., 2015. Influence of mixing layer height on air pollutant concentrations in an urban street canyon. Urban Clim. 1–13. https://doi.org/10.1016/j.uclim.2015.11.001
Walters, D., Boutle, I., Brooks, M., Melvin, T., Stratton, R., Vosper, S., Wells, H., Williams, K., Wood, N., Allen, T., Bushell, A., Copsey, D., Earnshaw, P., Edwards, J., Gross, M., Hardiman, S., Harris, C., Heming, J., Klingaman, N., Levine, R., Manners, J., Martin, G., Milton, S., Mittermaier, M., Morcrette, C., Riddick, T., Roberts, M., Sanchez, C., Selwood, P., Stirling, A., Smith, C., Suri, D., Tennant, W., Luigi Vidale, P., Wilkinson, J., Willett, M., Woolnough, S., Xavier, P., 2017. The Met Office Unified Model Global Atmosphere 6.0/6.1 and JULES Global Land 6.0/6.1 configurations. Geosci. Model Dev. 10, 1487–1520. https://doi.org/10.5194/gmd-10-1487-2017

Wandinger, U., Ansmann, A., 2002. Experimental Determination of the Lidar Overlap Profile with Raman Lidar. Appl. Opt. 41, 511–514. https://doi.org/10.1364/AO.41.000511
Wang, W., Gong, W., Mao, F., Pan, Z., Liu, B., 2016. Measurement and study of lidar ratio by using a Raman lidar in central China. Int. J. Environ. Res. Public Health 13. https://doi.org/10.3390/ijerph13050508
Warren, E., Charlton-Perez, C., Kotthaus, S., Lean, H., Ballard, S., Hopkin, E., Grimmond, S., 2018. Evaluation of forward-modelled attenuated backscatter using an urban ceilometer network in London under clear-sky conditions. Atmos. Environ. 191, 532–547. https://doi.org/10.1016/j.atmosenv.2018.04.045
Wiegner, M., Gasteiger, J., 2015. Correction of water vapor absorption for aerosol remote sensing with ceilometers. Atmos. Meas. Tech. 8, 3971–3984. https://doi.org/10.5194/amt-8-3971-2015
Wiegner, M., Madonna, F., Binietoglou, I., Forkel, R., Gasteiger, J., Geiß, A., Pappalardo, G., Schäfer, K., Thomas, W., 2014. What is the benefit of ceilometers for aerosol remote sensing? An answer from EARLINET. Atmos. Meas. Tech. 7, 1979–1997. https://doi.org/10.5194/amt-7-1979-2014
Ye, X., Tang, C., Yin, Z., Chen, J., Ma, Z., Kong, L., Yang, X., Gao, W., Geng, F., 2013. Hygroscopic growth of urban aerosol particles during the 2009 Mirage-Shanghai Campaign. Atmos. Environ. 64, 263–269. https://doi.org/10.1016/j.atmosenv.2012.09.064
You, W., Zang, Z., Zhang, L., Zhang, M., Pan, X., Li, Y., 2016. A nonlinear model for estimating ground-level PM10 concentration in Xi'an using MODIS aerosol optical depth retrieval. Atmos. Res. 168, 169–179. https://doi.org/10.1016/j.atmosres.2015.09.008
Young, D.E., Allan, J.D., Williams, P.I., Green, D.C., Flynn, M.J., Harrison, R.M., Yin, J., Gallagher, M.W., Coe, H., 2015. Investigating the annual behaviour of submicron secondary inorganic and organic aerosols in London. Atmos. Chem. Phys. 15, 6351–6366. https://doi.org/10.5194/acp-15-6351-2015
Zappoli, S., Andracchio, A., Fuzzi, S., Facchini, M.C., Gelencsér, A., Kiss, G., Krivácsy, Z., Molnár, A., Mészáros, E., Hansson, H.C., Rosman, K., Zebühr, Y., 1999. Inorganic, organic and macromolecular components of fine aerosol in different areas of Europe in relation to their water solubility. Atmos. Environ. 33, 2733–2743. https://doi.org/10.1016/S1352-2310(98)00362-8
Zelenyuk, A., Cai, Y., Imre, D., 2006. From Agglomerates of Spheres to Irregularly Shaped Particles: Determination of Dynamic Shape Factors from Measurements of Mobility and Vacuum Aerodynamic Diameters. Aerosol Sci. Technol. 40, 197–217. https://doi.org/10.1080/02786820500529406
Zhang, Y., Zhang, Q., Cheng, Y., Su, H., Kecorius, S., Wang, Z., Wu, Z., Hu, M., Zhu, T., Wiedensohler, A., He, K., 2016. Measuring the morphology and density of internally mixed black carbon with SP2 and VTDMA: New insight into the absorption enhancement of black carbon in the atmosphere. Atmos. Meas. Tech. 9, 1833–1843. https://doi.org/10.5194/amt-9-1833-2016

7 Notation and abbreviations

aerFO	Aerosol forward operator
ALC	Automatic lidars and ceilometers
AOD	Aerosol optical depth
APS	Aerodynamic particle sizer
C_c	Cunningham slip correction factor
$C_{ext,aer}$	Aerosol species' particle extinction cross section
$C_{back,aer}$	Aerosol species' particle backscatter cross section
CH	Chilbolton
CIR	Complex index of refraction
CPC	Condensation particle counter
D	Particle diameter
$D_{dry,aer}$	Aerosol species dry particle diameter
D_a	Particle aerodynamic equivalent diameter
D_m	Particle mobility equivalent diameter
D_v	Particle volume equivalent diameter
$D_{wet,aer}$	Aerosol species particle diameter at ambient RH
DMPS	Differential mobility particle sizer
del.	Deliquescence relative humidity limit
EC	Elemental carbon
ECMWF	European Centre for Medium-Range Weather Forecasts
ERG	King's College London Environmental Research Group
eff.	Efflorescence relative humidity limit
$f_{ext,rh}$	Extinction enhancement factor
FO	Forward operator
IFS	Integrated Forecasting System
IQR	Inter-quartile range
g_{aer}	Aerosol species' particle physical growth factor with respect to water
g_{OC}	Organic carbon physical growth factor with respect to water
JULES	Joint UK Land Environment Simulator
LAQN	London Air Quality Network
LUT	Look up table
LUMO	London Urban Meteorological Observatory
m	Aerosol mass mixing ratio
m_0	'Standard' mass mixing ratio
m_{MURK}	MURK aerosol mass mixing ratio
m_{aer}	Aerosol species mass
medBE	Median biased error
MO	Met Office
N	Total particle number concentration for aerosol mode
N_0	'Standard' or climatological mean, total particle number concentration for aerosol mode
N_{aer}	Aerosol species' dry number distribution
N_{obs}	Non-speciated number distribution
N_{tot}	Total number of particles across all size bins
NK	North Kensington
NPL	National Physics Laboratory
nSD	Normalised standard deviation
NWP	Numerical weather prediction
n	Number of particles in bin
n_{aer}	Aerosol species refractive index
n_{water}	Refractive index of water
$n_{wet,aer}$	Aerosol species mixed partial refractive index with water
OC	Organic carbon
PM_{10}	Total mass of particles with diameter less than 10 μm
$Q_{ext,aer}$	Aerosol species particle extinction efficiency
$Q_{ext,dry}$	Dry particle extinction efficiency
R_s	Spearman correlation coefficient

R_P	Pearson correlation coefficient
RH	Relative humidity
r_0	'Standard' or climatological mean, dry mean volume particle radius for aerosol mode
r_g	Dry number geometric mean radius for aerosol mode
r_{md}	Dry mean volume particle radius for aerosol mode
r_v	Water vapour mass mixing ratio
S	Lidar ratio
SNR	Signal-to-noise ratio
s	Parameterised wet/dry hygroscopic growth state
UKV	UK Variable Resolution model
V	Volume
V_{aer}	Aerosol species volume
V_{tot}	Total aerosol volume
$V_{weight,aer}$	Aerosol species volume weighting
X_{aer}	Aerosol species' size parameter
z	Height
β	Backscatter
β_m	Forward modelled attenuated backscatter
β_o	Observed attenuated backscatter
ρ_{air}	Air density
ρ_{aer}	Aerosol species density
λ	Wavelength
$\sigma_{ext,aer}$	Aerosol species' particle extinction coefficient
$\sigma_{back,aer}$	Aerosol species' particle backscatter coefficient
χ	Dynamic shape factor

Appendix 1. Estimation of geometric mean radius from volume mean radius by aerosol mode

The geometric number mean radius (r_g) is calculated using linear regression and the dry mean volume radius (r_v) as r_g is not estimated by the aerFO (Figures A1.1 – A1.3). The dry geometric number mean radius (r_g) is calculated as (Hinds, 1999):

$$r_g = \frac{(\Pi\, D_i^n)^{1/N_{tot}}}{2} \qquad (2)$$

where D_i is the mid-point particle size in bin i, n is the number of particles in bin i and N_{tot} the total number of particles across all bins. Calculations are done for dry particles.

The dry mean volume radius (r_v) is:

$$r_v = \frac{\Sigma\,(dn_i/dlogD_i * dlogD_i * D_i^4)}{\Sigma\,(dn_i/dlogD_i * dlogD_i * D_i^3)} \qquad (3)$$

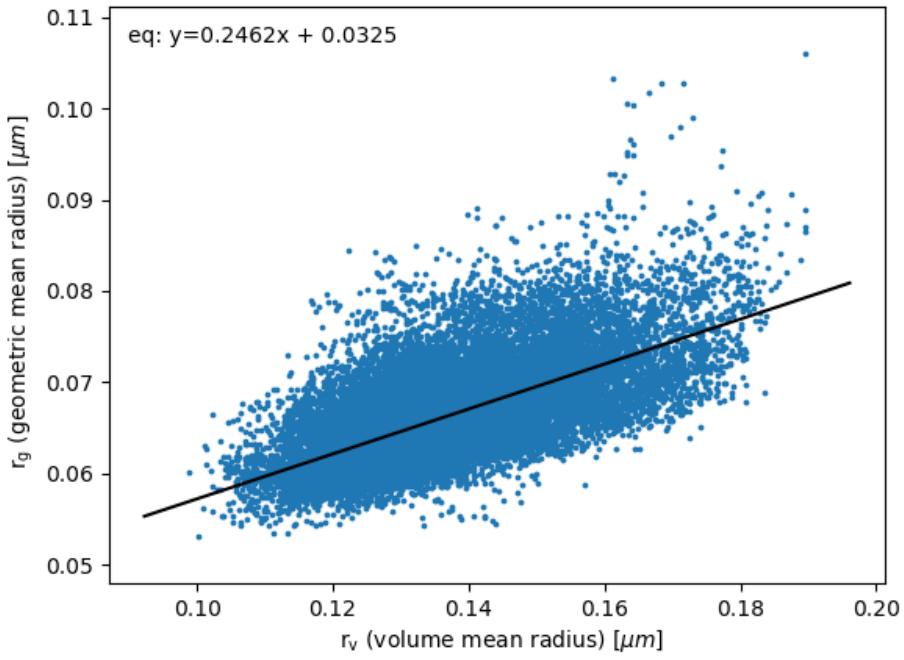

Figure A1.1: Observed dry geometric number mean radius (r_g) with observed dry mean volume radius (r_v) for the accumulation mode (radius: 0.04 – 0.4 μm) at North Kensington (NK) 01/01/2014 – 12/31/2015, from combined TSI SMPS and APS data. APS data are 'dried' based on physical growth factors calculated from observed RH at KCL (section 2.1, Figure 1). Linear regression (line), Pearson correlation (R_P) = 0.65 and statistically significant > 99 %.

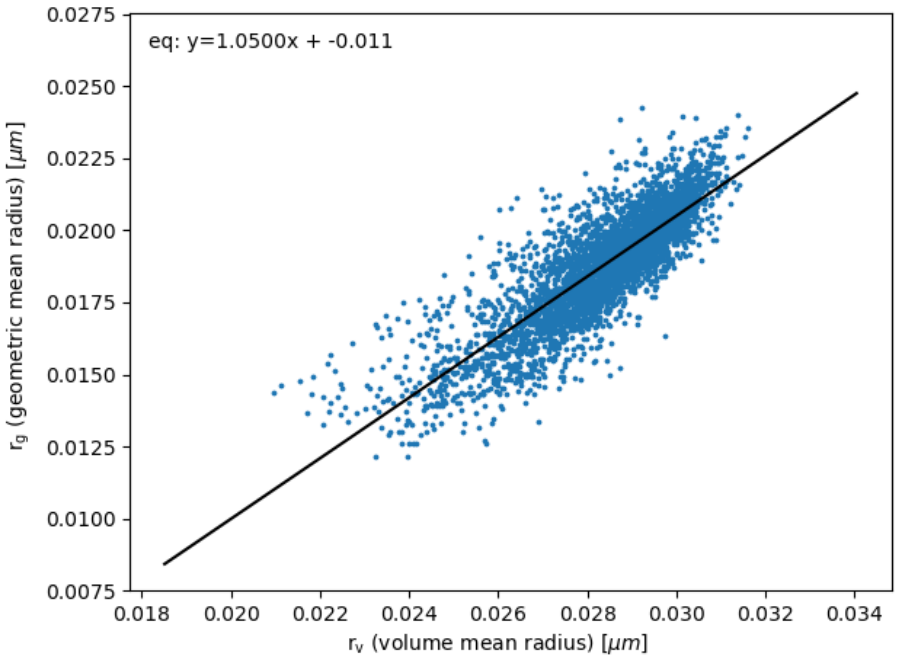

Figure A1.2: As Figure A1.1 but for fine mode (radii: < 0.04 μm). Pearson correlation (R_P) = 0.83 and statistically significant > 99 %.

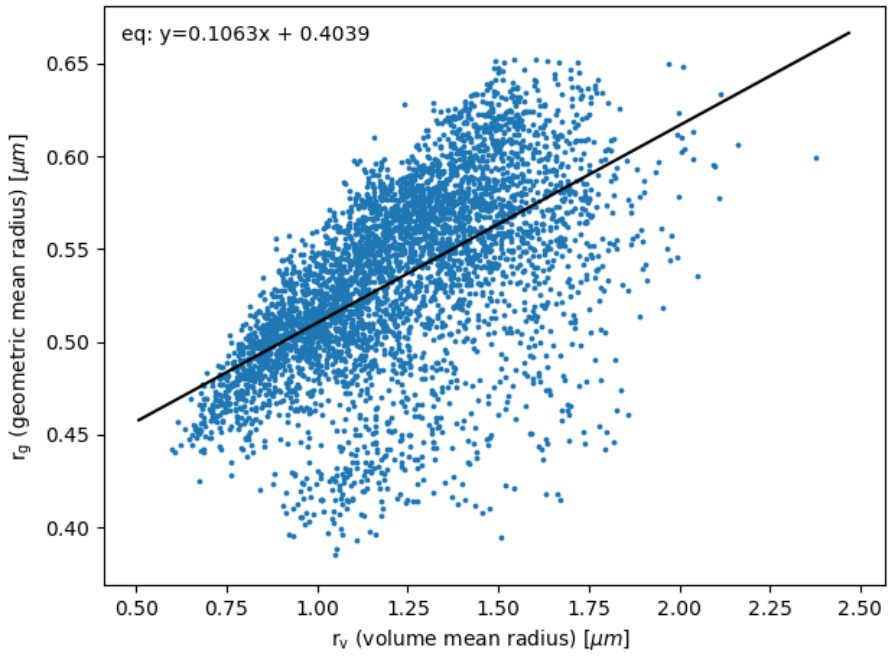

Figure A1.3: As Fig A1.1 but for the coarse mode (radii:> 0.4 μm). Linear regression (line), Pearson correlation (R_P) = 0.57 and statistically significant > 99 %.

Appendix 2. Extinction enhancement factor ($f_{ext,rh}$)

Because bulk aerosol optical properties vary strongly based on the hygroscopic properties, and the relative proportion of different aerosol species present (Warren et al., 2018), it is useful to understand how the common urban aerosol species contribute to extinction enhancement factor $f_{ext,rh}$ calculations.

Daily mean $f_{ext,rh}$ are estimated from hourly observed aerosol species for three UK sites: North Kensington (urban, NK), Chilbolton (rural, Ch) and Harwell (rural, Ha), for a fixed r_{md} = 0.11 μm and a *RH* range of 0 – 100 %. $f_{ext,rh}$ is appreciably lower when the relative volumes of EC are greater (Figure A2.1). Across all sites the mean relative volume of EC is 7.25 %. The lower $f_{ext,rh}$ values (Fig. A2.1 red, EC relative volume 9 – 100 %) reflect the hygrophobic nature of EC which has a constant $f_{ext,rh}$ of 1.0. Hence, aerosol mixtures with greater volumes of EC have a lower combined $f_{ext,rh}$.

The reduction in $f_{ext,rh}$ is greatest at higher *RH* (Figure A2.1). As *RH* increases, $f_{ext,rh}$ increases exponentially for hygroscopic aerosols, but as $f_{ext,rh}$ for EC remains constant the exponential increase in $f_{ext,rh}$ of the total aerosol is limited. The variability in $f_{ext,rh}$ increases with *RH* associated with the increased variability in $f_{ext,rh}$ between different aerosol species at higher *RH* values (Warren et al., 2018). Greater relative volumes of sea salt lead to higher daily estimates of $f_{ext,rh}$ (not shown) due its highly hygrophilic nature. Greater relative volumes of OC are related to lower $f_{ext,rh}$ values (not shown). Though OC is not strongly hygrophobic, the relatively high-volume fractions (average 41.7 %) makes it proportionally important when computing the optical properties of the combined aerosol.

In section 3.1, the impact of hysteresis is discussed as it relates to calculation of *S*. The hysteresis effect is not accounted for in the $f_{ext,rh}$ parameterisation as SOCRATES (which is used) does not include this effect. We recognize that hysteresis should be considered in future computation of LUTs of $f_{ext,rh}$, to provide more realistic extinction enhancement.

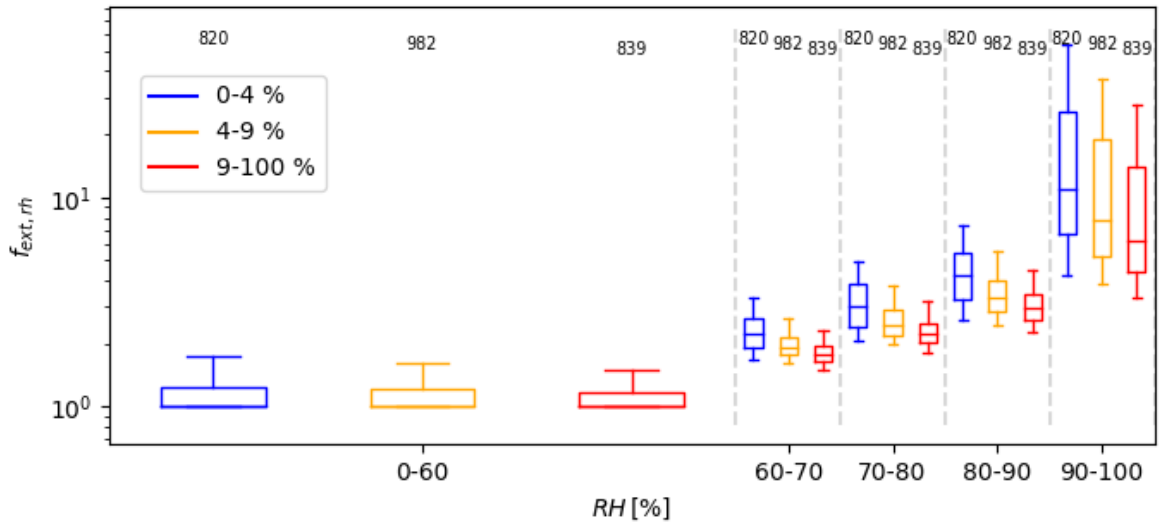

Figure A2.1: Modelled daily extinction enhancement factors ($f_{ext,rh}$) stratified by relative humidity (RH) [%] and relative volume of elemental carbon [%] using observed daily mean relative volumes of each aerosol species as input. Median, IQR, 5th and 95th percentile whiskers, and outliers (crosses) shown with sample size. Estimates calculated for 0 – 100 % RH for a radius of 0.11 µm using data from three sites: North Kensington (n=1378), Chilbolton (n=192) and Harwell (n=1071). Note log scale on y-axis.